

Review

Tungsten Heavy Alloys Processing via Microwave Sintering, Spark Plasma Sintering, and Additive Manufacturing: A Review

R. Manikandan¹ and A. Raja Annamalai^{2,*} ¹ School of Mechanical Engineering, Vellore Institute of Technology, Vellore 632014, India² Centre for Innovative Manufacturing Research, Vellore Institute of Technology, Vellore 632014, India

* Correspondence: raja.annamalai@vit.ac.in

Highlights:

- The dihedral angle and liquid content of WHA alloy greatly influence the alloy's density.
- High densification and deformation were observed in the sample with high liquid content and low dihedral angle.
- The mechanical characteristics of tungsten-heavy alloys improved by using 93 wt.%W.
- Various pressing and sintering procedures are correlated with powder size and relative density.

Abstract: Tungsten-heavy alloys (WHA) are a pseudo-alloy in which tungsten is the primary phase and remains filled with additives such as Ni-Fe and Ni-Cu. These alloys are widely used to make their applications' structural, electrical, and electronic components. According to this study, in addition to processing factors, the prime factors affecting the performance of WHAs are microstructural features such as tungsten and matrix composition, powders shapes and sizes, and distributions of tungsten particles in the matrix, as well as interface-bonding strength between the tungsten particle and matrix. This study summarises current developments in WHA processing, microstructure, and mechanical characteristics. For the manufacture of WHAs, various processing methods are discussed, including traditional powder metallurgy (PM), microwave sintering (MW), spark plasma sintering (SPS), and additive manufacturing (AM). SPS process depicts better results when compared with conventional sintering. This review will also hint at the effects of some additives in tungsten and their advantages.

Keywords: tungsten-heavy alloy; microwave sintering; spark plasma sintering; additive manufacturing



Citation: Manikandan, R.; Raja Annamalai, A. Tungsten Heavy Alloys Processing via Microwave Sintering, Spark Plasma Sintering, and Additive Manufacturing: A Review. *Processes* **2022**, *10*, 2352. <https://doi.org/10.3390/pr10112352>

Academic Editors: Junwu Tao, Kama Huang, Lionel Estel, Li Wu and Paola Ammendola

Received: 29 September 2022

Accepted: 5 November 2022

Published: 10 November 2022

Publisher's Note: MDPI stays neutral with regard to jurisdictional claims in published maps and institutional affiliations.



Copyright: © 2022 by the authors. Licensee MDPI, Basel, Switzerland. This article is an open access article distributed under the terms and conditions of the Creative Commons Attribution (CC BY) license (<https://creativecommons.org/licenses/by/4.0/>).

1. Introduction

With its high melting point, erosion resistance, and radiation-tolerance features, tungsten is used for many applications. Tungsten is the sole metal in electron emitters due to its low vapor pressure at high temperatures [1,2]. Because of its high density, it is utilized in structural application as balance weights, rotating inertia parts, and oscillating weights. Conventional WHAs such as W-NiCu and W-NiFe were developed in the 1930s and newer WHAs such as W-Ni-(Co, Mn, Nb) alloys have emerged in recent decades. WHA performance is mainly determined by its compositions and manufacturing conditions. In past decades, optimization of WHA's composition and sintering cycle was made by several researchers to achieve high-performance WHA. This study overviews current advancements in tungsten-heavy alloy fabrication and alloy additives. Sintering processes such as spark plasma, microwave, and additive manufacturing are discussed in this article.

1.1. Hydrometallurgical Process of Tungsten

Figure 1 shows the schematic representation of the hydrometallurgical process of tungsten. Wolframite and scheelite are the two primary forms of tungsten ores, and each

has unique properties [3]. Wolframite, huebnerite, ferberite, and scheelite are examples of minerals in which tungsten naturally occurs. Ferberite is the iron endmember of the iron—manganese wolframite solid solution series and is composed of iron-rich tungstate (FeWO_4 WO_3 content = 76.3%). Manganese endmember is huebnerite and it is composed of manganese-rich tungstate (MnWO_4 WO_3 content = 76.6%). The combination of manganese and iron endmember presence in wolframite is composed of iron—manganese-mixed tungstate ($(\text{Fe}, \text{Mn}) \text{WO}_4$, WO_3 content = 76.5%). In addition, commercial production of W entails a chemical procedure to obtain ammonium para-tungstate from mineral concentrate. Ammonium meta-tungstate, W-blue oxide, and W-yellow oxide are the intermediates among tungstate's constituents. Tungsten oxides are reduced by hydrogen to form tungsten metal particles. Tungsten powders with diverse characteristics can be made through optimizations in the hydrogen reduction process.

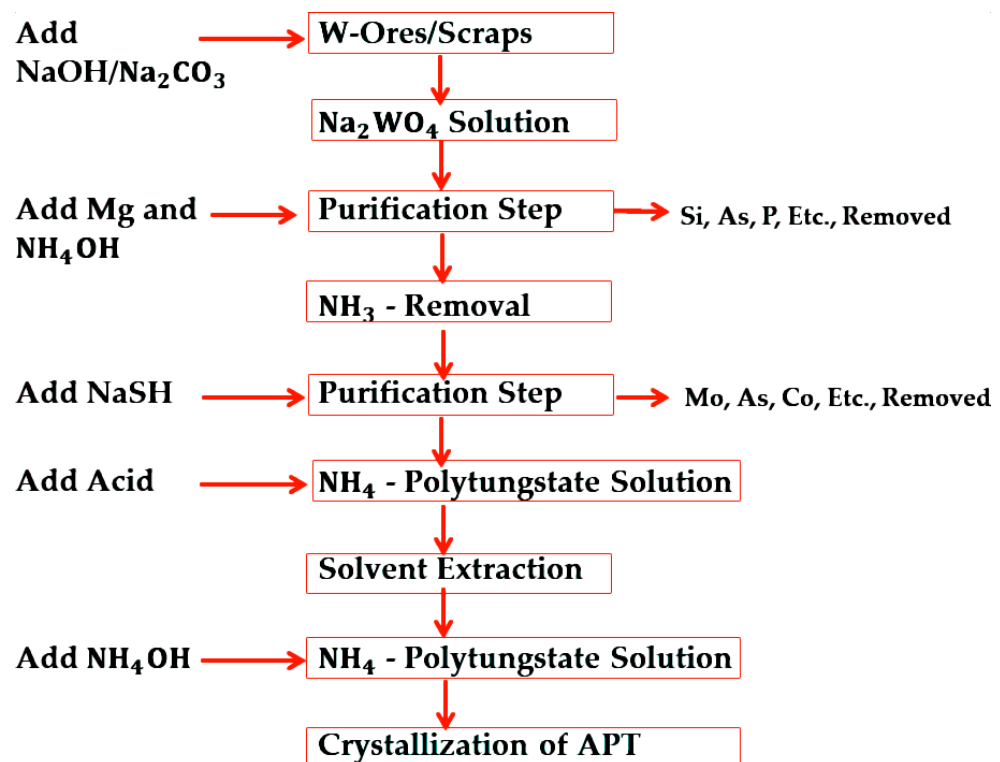


Figure 1. Flow diagram of tungsten hydrometallurgical process [3].

1.2. Tungsten-Based Alloys and Their Applications

Tungsten alloying improves its chemical, physical, and mechanical properties at low and high temperatures. Some essential tungsten-based alloys are discussed here. The high brittleness nature of tungsten at low temperature causes difficulties during fabrication. However, in W–Re alloys, the transition temperature from ductile to brittle is significantly reduced, making W fabrication easier. Adding Re to W improves the alloy's creep, ductility, and corrosion resistance [4]. Engineers used this W–Re alloy in thermocouples to monitor engine combustion chambers, furnaces, and reactors that reach 2600 °C. W–5Re and W–3Re/W–25Re are two of the most regularly utilized W–Re alloys in thermal element applications [5]. Tungsten's remarkable hot strength is combined with tantalum's flexibility and corrosion resistance in W–Ta alloys. These alloys are used in corrosive environments as building materials [6,7]. There are numerous ways in which nuclear fusion technology might assist humanity. In the nuclear field, W–Mo alloy depicts enhancement in its plasma facing performance by reducing neutron irradiation and heat flux. Moreover, W–Mo alloy showed consistent fracture across the limiter at lower temperatures than pure W metal [8]. In the electronic field, microelectronic devices use W–10Ti alloys as sputter targets. Ad-

ditionally, W–Ti alloys can be used in nuclear reactors as PFM materials because of their remarkable thermal stability at high temperatures [9]. W–Ag alloys have high potential due to tungsten’s high wear resistance-cum-hardness and silver’s electrical conductivity [10,11]. W–Ag has applications such as arcing contacts in medium-voltage circuit breakers and welding electrodes. Additionally, various alloys are utilized in radar technology, electronics packaging, and other applications [12]. W-based alloys find use in many industries, as seen in Table 1.

Table 1. Applications of W and its alloys in various fields.

Composition	Application	Reference
W–25Re	Rocket engine ignition tubes, thermionic emitters on spacecraft.	[5]
W–Ta	Building materials for corrosive environments	[6,7]
W–Mo	Irradiation shielding material in nuclear application	[8]
W–10Ti	Sputtering target in microelectronic devices.	[9]
W–Cu	Arcing contacts in circuit breakers	[10]
W–Ag	Heat sink devices in the electronic industry	[11]

Tungsten-Heavy Alloy (WHA)

WHA is a two-phase composite in which tungsten is spread in a nickel-based binder matrix. Powder metallurgy is the most common method used to produce WHA because of its high melting point [13,14]. Tungsten grains often contain a ductile matrix phase in these two-phase alloys. The nickel-based binder matrix may contain transition metals such as Co, Cu, and Mn. A wide range of engineering applications can benefit from tungsten’s strong strength, corrosion resistance, and exceptional wear resistance. It is utilized as balance weights, rotating inertia parts, and oscillating weights because of its high density. Tungsten is an ideal radiation shielding material in nuclear reactors because of its remarkable capacity to absorb X-rays and gamma radiation [15]. Tungsten is an excellent choice for lamp filament, X-ray detectors, and contact material for high-frequency switches. The sole material employed in electron emission is W because of its low vapor pressure at high temperatures [16]. W is also used in nuclear applications as a gamma radiation shielding material and as a kinetic energy penetrator [17]. There have been several techniques used to achieve near-theoretical density and high mechanical characteristics via the PM process over the last few decades. The latest advances in W–Ni–Cu, W–Ni–Mn, and W–Ni–Fe are the primary emphasis of this article.

1.3. Powder Metallurgy

Powder metallurgy is the primary method for processing tungsten metal powder. In 1909, W. D. Coolidge filed a patent application with the United States Patent Office. The PM technique was used to make tungsten wire, detailed in the patent [18]. Powder metallurgy’s genetics were revolutionized by this method. Tungsten production in the industrial sector has changed, but the PM process is still widely used to make tungsten around the world. In addition, the PM process was used to manufacture 75% of the world’s tungsten. Compaction and sintering are two of the most critical stages in the PM process. The Isostatic press (uniaxial press) uses a flexible mould and a rigid die to compact tungsten powder into a compact form. A billet is formed by pressing powder into a die in a uniaxial or a biaxial die press. Compaction pressure is typically between 100 and 400 MPa. The compact density ranges from 55% to 66% of theoretical density depending on the powder’s shape, size, and applied pressure [19]. It is possible to connect applied pressure to green density using numerous theoretical formulae. In practice, the use of empirical relationships is quite usual.

In most cases, the final moulding is robust enough to handle without breaking. Subsequently, the sintering process takes place in the material. The powder particles are combined and become one solid mass in the sintering process. Densification occurs when pressure and heat are applied to a powdered material, owing to a loss in surface energy and

a variety of atomic processes such as diffusion, plastic flow, viscous flow, and evaporation between the powder particles. During the sintering process, the component gains density via either self-resistance or resistance element heating [20]. Sintered pieces might be varied via metal work and heat treatment depending on the requirements of the final product.

2. Manufacturing of Pure Tungsten

Figure 1 depicts the hydrometallurgical method used to extract the tungsten mineral from the ore material. Crushing, gravity separation, and flotation are all part of this procedure. It is necessary to convert APT into a tungsten oxide to use it as a catalyst (WO_3). This tungsten trioxide can be reduced to pure W metal powder via hydrogen reduction [21]. Table 2 summarizes the factors that affect tungsten particle compaction. Irregular-shaped particles are stronger but less dense than regular-shaped particles.

Moreover, when pressure is applied, significant friction between particles produces finer powders with a lower compact density. Typically, PFM material requires pore-free material with high toughness. In the past decades, several techniques have been used to make fully dense parts. Hot-pressing with parameters such as 1300 °C temperature and 30 MPa pressure for densifying tungsten and carbon yields a completely dense material within 12 min. Fully densified tungsten shows its potential for plasma facing material application [22]. At elevated temperatures, tungsten metal has a greater chemical affinity for carbon, resulting in WC. The diffusion of carbon from graphite in the die material can lead to tungsten—carbide formation, according to numerous studies [23,24]. Because tungsten is pressed, it is impossible to avoid the incorporation of carbon into the tungsten component.

Regarding tungsten and carbon, it is essential to look into ways to stop or reduce their interactions. According to McCarty et al., the carburization rate decreases as the particle size increases. The longer it takes to carburize, the larger the particle size, and the longer it takes to finish the process. Refractory material can provide a barrier between graphite and tungsten to lower both the depth of carburization and the thickness of the carbide layer [25]. Evidence suggests that zirconium and niobium carbide are the best anti-diffusion block materials [26,27]. Carburization of tungsten can almost be eliminated using materials like zirconium dioxide and boron nitride on the graphite, and a tungsten working surface. Boron nitride in particular has been shown to reduce carbon diffusion during SPS. Gomez et al.'s study reveals the effect of boron nitride coating on Graphite foil. In their research, the inner foil of graphite dies was coated with boron nitride before loading the powder. When boron nitride-coating graphite paper, the WC layer thickness was 191 nm. It was also found that in the case that was not coated with boron nitride, there was an extra layer of WC with a thickness of 253 m. Carburization was reduced only to a limited extent.

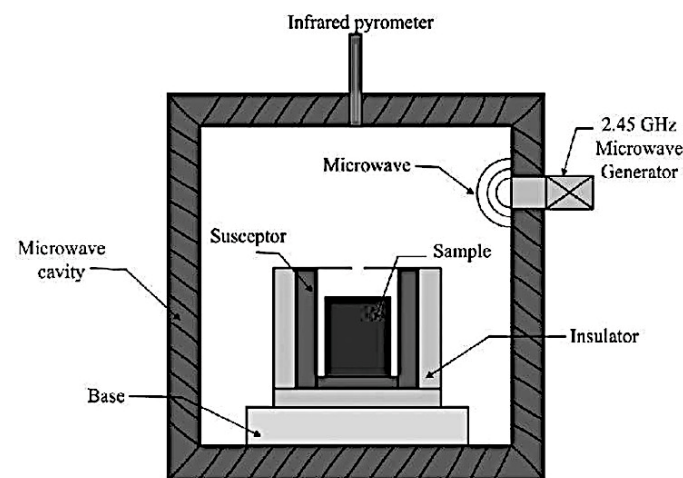
Regarding tungsten, the increased solubility of carbon could explain the lack of control [28]. On the other hand, tungsten is extremely sensitive to changes in oxygen content when exposed to both high temperatures and low levels of oxygen. Due to the formation of tungsten oxide layers at the tungsten/binder contact, it may cause performance deterioration when used in nuclear applications [29,30]. Typically, characteristics such as the powder's purity, shape, compact size, density, sintering environment, heating and cooling rates, sintering activators, and thermal gradient affect sintering densification. The most important variables in determining sintering kinetics are particle size, sintering duration, and temperature. The sintering temperature is raised to reach high densities quickly [31]. Table 2 shows the effect of particle size on compact density. Tungsten compacts may now be made at lower temperatures and faster because of advances in powder processing technology. Additive manufacturing of metal powders is currently being developed.

Table 2. Effect of powder size on relative density of W.

Powder Particle Average Size (Microns)	Mode of Pressing	Compaction Pressure (MPa)	Compact Density (% Theoretical Density)	Mode of Sintering	Sintering Temperature (°C)	Holding Time	Sintered Relative Density (%Theoretical Density)	References
0.7 (Cold press 1)	Cold isostatic pressing	255	44.85	MW & HIP	1500	20 min	93	[31]
0.41 (Cold press 2)	Cold isostatic pressing	255	48.2		1500		98.5	[31]
0.16 (EP1)	Cold isostatic pressing	255	62.96		1500		75	[31]
0.5 (EP2)	Cold isostatic pressing	255	34.97		1500		93	[31]
5–50 (CP)	Cold isostatic pressing	250		Microwave	1600	1 h	85.49	[31]

2.1. Synthesis of WHA Microwave Sintering

Microwaves are a type of energy that contain an orthogonal magnetic and electric field that can be used for various purposes, including heating and cooking. Typically, metals cannot absorb microwaves in their solid state, but they can be absorbed when they are powdered. Microwave sintering considerably enhances the pace of reactions, kinetics of diffusion, sintering duration, and fine microstructures, leading to superior products and significant energy savings. Figure 2 shows schematic of microwave sintering furnace.

**Figure 2.** Schematic of microwave sintering furnace [32].

Microwave sintering has a significant advantage over other methods. Thermal conductivity includes heat transfer modes such as radiation and convection followed by conduction in conventional sintering. Thermal equilibrium and consolidation of the materials take a long time in traditional sintering. It is important to note that in microwave heating, the microwave field is absorbed first before the electromagnetic energy is converted into thermal heat. No heat transfer modes were used in this procedure because the heating was instantaneous and highly dependent on the material's pace. When the heat is produced internally and delivered outward, it does not come from outside. Rather than heating from the outside in, the heating profile is reversed from the inside out. Microwave heating is much faster than traditional methods because it uses energy conversion rather than transmission to heat the material. Figure 3 shows heating profiles of conventional and microwave sintering.

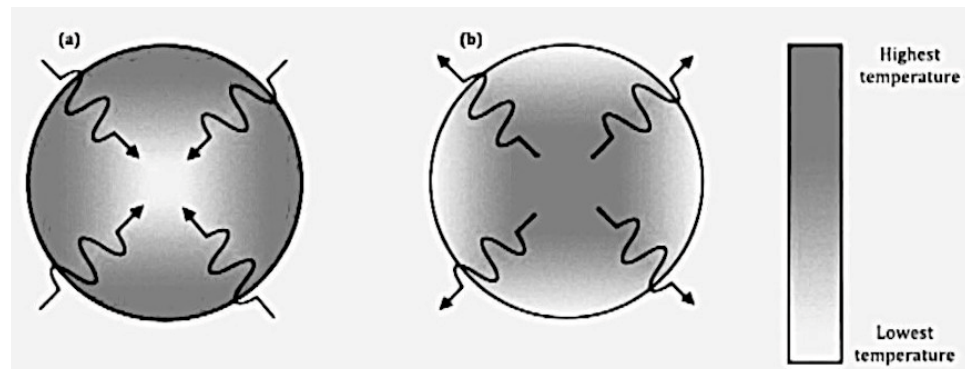


Figure 3. Heating profiles in (a) conventional, (b) microwave [33].

In 1988, Roy et al. discovered microwaves to sinter metal powder. Table 3 shows the effect of powder size on relative density [34]. Jain et al. focused on tungsten powders (average particle sizes of 0.16, 0.50 μm) in microwave sintering. However, green density is higher; small powder particles do not assure high sintering density. It shows that a combination of particle characteristics controls the behaviour of densification. In addition, it indicates that microwave-sintered tungsten has a density increase of 12–18% over traditional sintering [35]. In a similar environment, Prabhu et al. [36] investigated the sintering of W (5–50 μm) and milled W powder (1–3 μm). Microwave sintering was used with temperatures ranging from 1600 $^{\circ}\text{C}$ to 1800 $^{\circ}\text{C}$ and a holding duration of one hour. Commercial tungsten powder (5–50 μm) milling was carried out for 5 h in water medium in a planetary mill. Grinding medium: tungsten carbide, ball to powder ratio: 5:1, speed ratio of mill 2.88, plate and bowl speed of 240 rpm and 670 rpm, respectively. There was no sign of densification in commercial-grade powder at any of the three temperatures evaluated in this investigation.

Table 3. Heating rate effects in 90W-7Ni-3Fe-heavy alloy.

Modes of Sintering	Rate of Heat ($^{\circ}\text{C}/\text{min}$)	Sintered Relative Density (g/cm^3)	Yield Strength (YTS) (MPa)	Tensile Strength (UTS) (MPa)	Elongation (%)
Conventional	5	16.97 ± 0.02	605 ± 15	862 ± 12	19.68 ± 1.4
	10	16.92 ± 0.04	575 ± 23	810 ± 44	12.78 ± 4.5
	20	17.03 ± 0.01	585 ± 10	858 ± 61	19.24 ± 0.7
	29	16.96 ± 0.04	613 ± 22	877 ± 18	23.04 ± 1.3
Microwave	45	17.02 ± 0.01	610 ± 25	623 ± 17	21.02 ± 0.2
	65	16.91 ± 0.04	887 ± 81	898 ± 32	20.92 ± 1.3
	80	17.04 ± 0.01	629 ± 15	923 ± 24	19.72 ± 2.2
	90	17.03 ± 0.01	611 ± 33	879 ± 22	20.23 ± 1.1
	105	17.01 ± 0.02	568 ± 23	852 ± 32	21.44 ± 2.6

On the other hand, milled W powder has a sintered density of 18 g/cc at 1800 $^{\circ}\text{C}$ [36]. Mondal et al. [37] used conventional and microwave sintering in a hydrogen atmosphere to investigate tungsten powder (average size 72 nm). Figure 4 compares the heat profiles of compact sintered utilizing both methods. Microwave sintering reduces the overall advancement time by about 90%. An experimental study focused on microwave and conventional sintering. In case of SPS, the heat profile will have the combined effect of joule heat and plasma heat. Nanoparticle sizes have also been shown to improve compaction during low-temperature sintering. A relative sintered density of 95 percent is achieved at 1600 $^{\circ}\text{C}$, more significant than the 1800 $^{\circ}\text{C}$ values of Prabhu et al. [36].

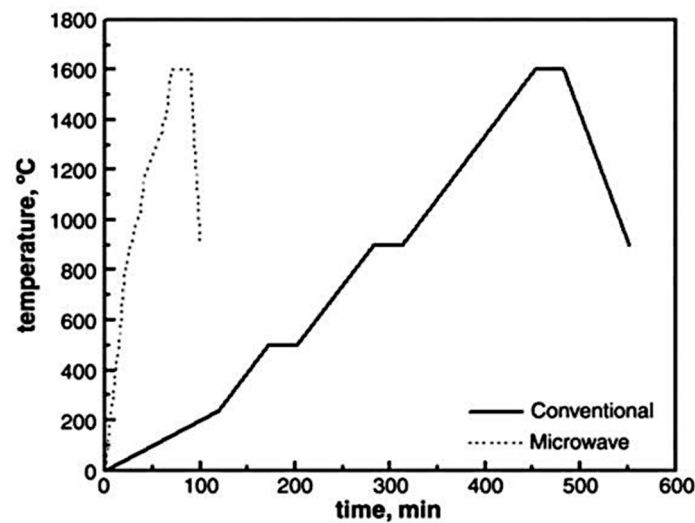


Figure 4. Comparison of the thermal profiles: conventional and microwave [37].

Figure 5 depicts the microstructures of conventional and microwave-sintered compacts. Compared to the microwave-sintered compact, the conventionally sintered compact appears coarser. However, due to the high heating rates in the microwave furnace, the microstructure coarsening was comparatively modest. Consequently, microwave-sintered compacts have better mechanical characteristics than those produced by traditional sintering.

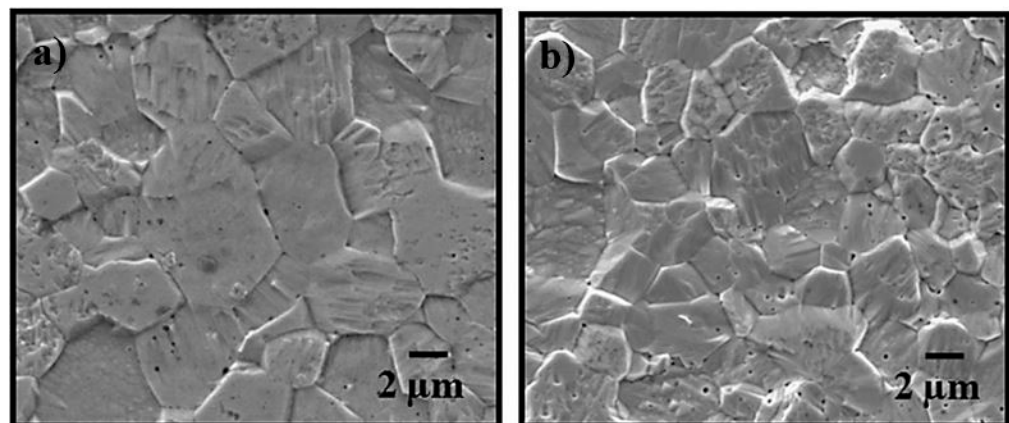


Figure 5. SEM micrographs: (a) conventional sintering and (b) microwave sintering [37].

The milling process of powders might enhance the sintering process. However, the formation of impurities during the milling process is a concern. Microwave sintering of tungsten powders (sizes of 20–100 nm and 3 nm) at a temperature of (1400–1500 °C) for 30 min was the focus of Wang et al.'s study. Milling was carried out for 12 h at 240 rpm in tungsten carbide and stainless-steel vials. Impurities such as Fe and Cr grew throughout the ball-milling process in stainless steel ball milling, which is shown in Figure 6. Fe₇W₆ contaminant in the sample was discovered in XRD analysis, which is represented in Figure 6. The samples sintered from the steel-ball-milled micrometre W powders have densities between 17 and 17.3 g/cm³, which is significantly less than the densities of the powders made from the tungsten carbide vial. Even though Fe impurity is an efficient sintering catalyst that can increase the sintering density of W samples to some extent, the introduction of several such impurities with much lower densities would cause the total density of the sample to decrease. Thermal conductivity (κ) was calculated from the relationship: $\kappa = c\rho\alpha$, where c is the heat capacity and ρ is the actual density. The value of c was taken as 0.13 J/gK in this study. Figure 7 shows thermal conductivity for both carbide and stainless-steel ball milling. The material imperfections increased grain coarsening and reduced thermal

conductivity. On the other hand, tungsten carbide ball milled powder has a high thermal conductivity due to absence of impurities during milling [38].

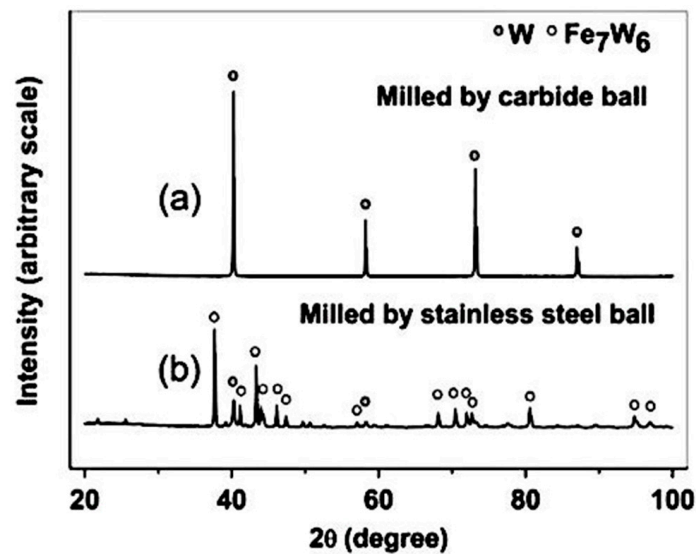


Figure 6. XRD profiles of tungsten by MW process [38].

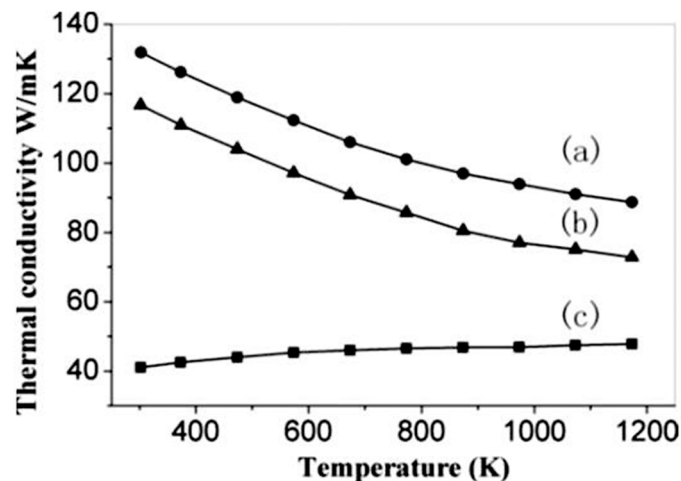


Figure 7. Thermal conductivity: (a) carbide ball mill W powders (nm), (b) carbide ball mill W powders (micron), (c) SS-ball milled W powders (micron) [38].

Though microwave sintering is used to synthesize WHA, electrical conductivity dip in the material becomes a crucial concern in microwave sintered parts. This is because the skinning effect during fabrication in microwave sintering causes a dip in the electrical conductivity of the sintered part. Therefore, spark plasma sintering is used to synthesize WHA. Also, SPS's heating rate is higher, which offers enhanced properties in the sintered parts.

2.2. Synthesis of WHA Spark Plasma Sintering

Sintering metal powder compacts using spark plasma has become popular in recent years. Figure 8 depicts a simple representation of SPS's fundamentals, as depicted in several reports. Powders are compacted with the help of high-voltage DC pulses and high pressure (30–100 MPa). It is thus possible to sinter the samples with a faster heating rate in 30 min, as opposed to conventional sintering, in which the sample is heated from the outside. A graphite die was used to bond the packed particles in the SPS process. Die, powder, and punch all used graphite foils to make sample removal from the die much easier. A pulsed

current and pressure are supplied to the powder simultaneously. Figure 9 depicts the neck formation mechanism in SPS process.

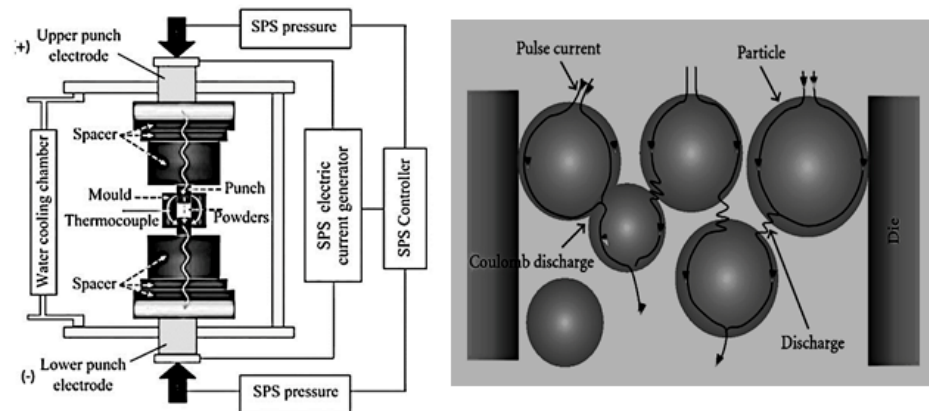


Figure 8. Schematic illustration of the features of SPS [39].

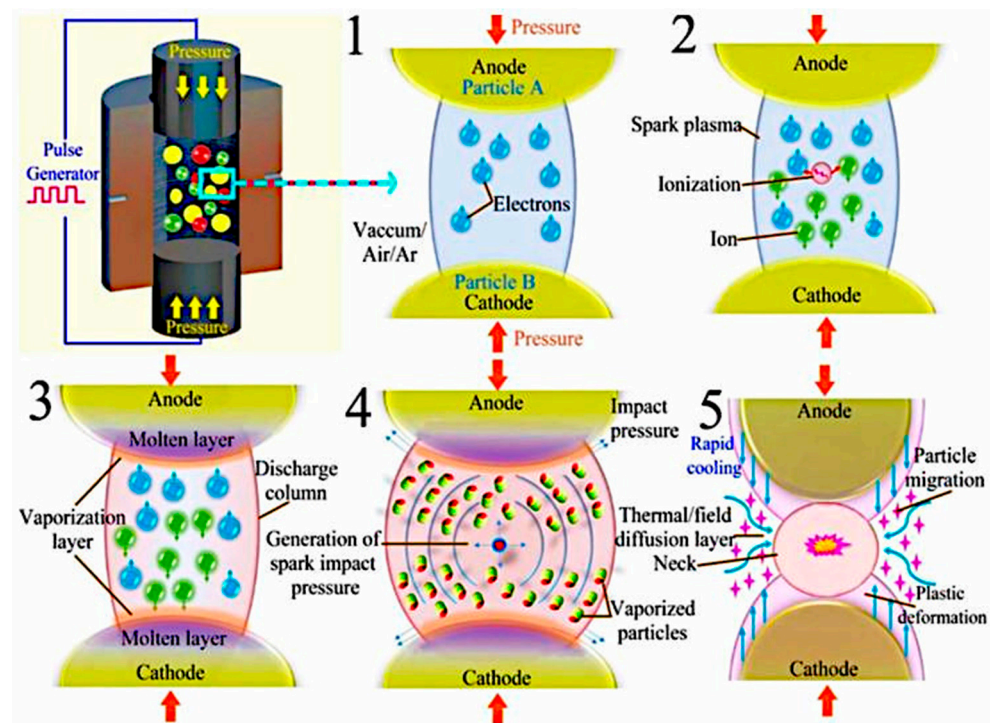


Figure 9. Neck formation mechanism in SPS Process [40].

In 1999, Tokita et al. studied the physics of spark plasma sintering. To summarise, he found that the sintering process is divided into five distinct stages: (1) discharging arcs, (2) generating plasma, (3) evaporating and melting, (4) applying impact pressures, and (5) neck formation. Using the SPS method, a more rapid consolidation rate is achieved, as depicted in Figure 9, which explains how the neckline forms through plasma generation, joule heating, DC pulsed current, and mechanical pressure [41–43].

During the first stage, the ON–OFF pulse energization liberates the space between the particles, allowing them to move freely. Spark plasma is created in the second stage. As a result, powder particles may melt and evaporate in the third stage because of the high temperature. Spark impact pressure arises in the fourth stage as a result of sputtering. Finally, necks are formed because of the diffusion of particles on the surface of the plasma.

Electrical discharge between powder particles causes localised, instantaneous heating of the particle surfaces to temperatures of up to several thousand degrees Celsius. The pro-

duced heat is spread consistently across the sample volume due to the uniform formation of the micro-plasma discharges. The high temperature that causes the vaporisation of the pollutants that are concentrated on the particle surface purifies and activates the particle surfaces. In order to generate “necks” between the particles, the refined surface layers of the particles melt and merge with one another. At this moment, the necks connecting the particles allow the pulsed DC current to flow from particle to particle. Electrical current produces joule heat. The joule heat increases the diffusion of the atoms/molecules in the necks, enhancing their growth. Rapid temperature increase and fall are made possible by the heating’s localised nature and homogenous distribution, which reduces material grain development and coarsening. Under the influence of a uniaxial force, the heated material deforms plastically and becomes softer. The powder compact is densified to over 99% of its theoretical density as a result of plastic deformation and diffusion.

The sintering of pure tungsten powder with a mean particle size of 0.5 nm was studied by Viola et al. In the SPS furnace, the powder was first cold crushed to a force of 5 kN. Sintering begins at 2100 °C at a rate of 100 °C/min. The density curve was shown as a function of temperature and relative density (refer to Figure 10). Tungsten is subjected to a compressive at a temperature between 1250 and 1500 °C. As a result, SPS can achieve a high tungsten compaction density (97% theoretical) without utilizing additional materials, according to the experiment’s results. [44].

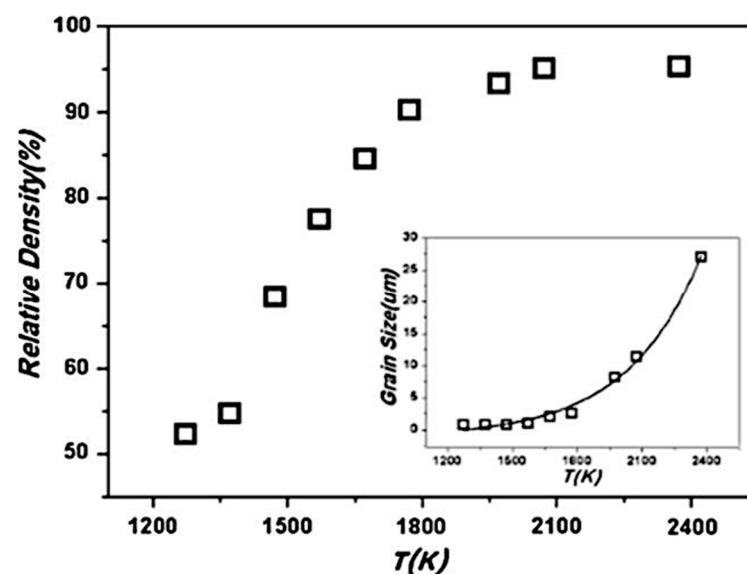


Figure 10. Densification curve of tungsten with various temperatures [44].

The effect of heating rate in SPS mainly controls the diffusion mechanism. For the specimens sintered with heating rates less than 100 °C/min densification occurs mainly through a combination of dissolution–precipitation of W through the matrix phase and W grain boundary diffusion. However, specimens sintered with heating rates higher than 100 °C/min—the apparent activation energy value for the mechanism controlling densification is a strong function of the relative density—and fast densification controlled by multiple diffusion mechanisms and intensive viscous flow dominates over the grain growth. This suggests that a high SPS heating rate is favourable for obtaining high density and fine-grained tungsten-heavy alloys [45].

In an argon atmosphere, mechanical alloying was also utilized by Villanova et al., who analysed three different forms of tungsten powders. One had two-micron tungsten particles, while the other two were treated with Y₂O₃ in a planetary ball mill. Ball-milled tungsten was other option. The milling was conducted for 25 h at 240 rpm in a WC vial. Subsequently, SPS technique was used to solidify the powders at 1800 °C and 70 MPa

pressure for 2 min. This study found that the addition of yttria particles significantly influenced the hardness of the materials.

Furthermore, the thermal conductivity of the tungsten-milled sample increased significantly. Increasing the material's heat conductivity significantly would positively affect its fusion behaviour [46]. As with traditional sintering, higher heating rates are feasible with SPS because the sample is heated within the die rather than outside. When the temperature and heating rate increase, the material's densification (i.e., reduction in surface energy) may increase between the particles. As previously stated, the findings of Hu et al. confirm the concept. In their study, the SPS technique was used to sinter tungsten-heavy alloy W-5.6Ni-1.4Fe at temperatures ranging from 870 °C to 1410 °C, with varying heating rates [47]. The entire process was divided into three stages based on the heating rate. Solid-state powders experience a rapid release of temperature distribution across particle contacts in the preliminary stage (below 900 °C) due to a higher heating rate. It is also during this intermediate stage (900–1320 °C) that densification occurs in solid-state sintering. A rapid coarsening of tungsten occurs at the penultimate step (1320–1410 °C). Faster heating also results in smaller tungsten grains being formed during liquid-phase sintering. As seen in Figure 11, samples heated at slower and quicker heating rates show a substantial change in relative density. At 1320–1380 °C, the relative density of a heated specimen heated at 90 °C/min remains constant. A rise in temperature in the liquid phase raises the relative density of the liquid phase.

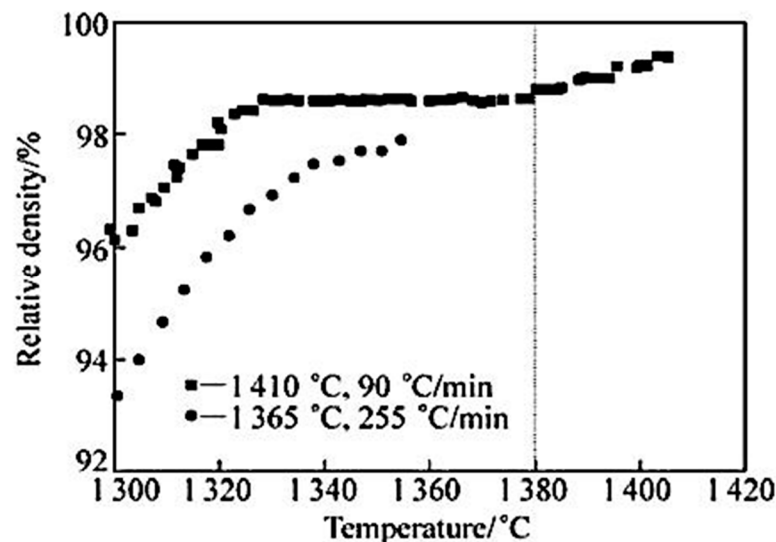


Figure 11. Relative density with sintering temperature [47].

High-current samples had a bigger experimental-to-real temperature discrepancy in the middle position. Temperature gradients in the LPS process changed due to the increased applied current. Different temperatures can't be controlled at a pace of 90 °C/min in the LPS process. This development can be summarised as follows: Wetting the tungsten particles first helps to distribute the temperature. Later, the solid particle dissolve in the liquid pool, causing them to decrease and reorganize as they dissolve. Finally, the pores between the particles are filled with the melted liquid. Densification, the process by which tungsten particles become spherical due to a reduction in the interfacial energy, eventually occurs.

2.3. Synthesis of WHA Additive Manufacturing

In the past decades, some standard production procedures used to make tungsten-based powder components were metal injection moulding, powder metallurgy, and hot isostatic pressing [48]. Spraying techniques can deposit thin tungsten films, including physical and chemical vapour depositions. These methods are useless because tungsten is brittle at room temperature, making them unproductive for manufacturing complex

tungsten objects. Due to the coarsening of ultrafine nanostructures during PM processing, a heterogeneous microstructure was produced [49,50]. Due to the factors above, AM (additive manufacturing) appears to be a viable option for tungsten production. Tungsten and tungsten-based materials have been produced via AM methods such as laser powder bed fusion, electron beam powder bed fusion, direct energy deposition, and bonded metal deposition. Laser powder bed fusion is a commonly used method for printing tungsten-based materials. The 3D model is divided into layers using specialized software in the additive manufacturing process. Layer by layer, the 3D model is printed from sliced digital files. Inherent properties, including thermal conductivity, surface tension, and laser energy absorption rate play a role in an alloy's suitability for additive manufacturing. Thermal conductivity is generally inversely proportional to the input energy dissipation. Incomplete melting and the wettability of melt pools and solid particles are affected by high heat conductivity and a rapid solidification rate. The higher the solidification rate, the greater the chance of cracking. The L-BPF process is shown schematically in Figure 12 [51].

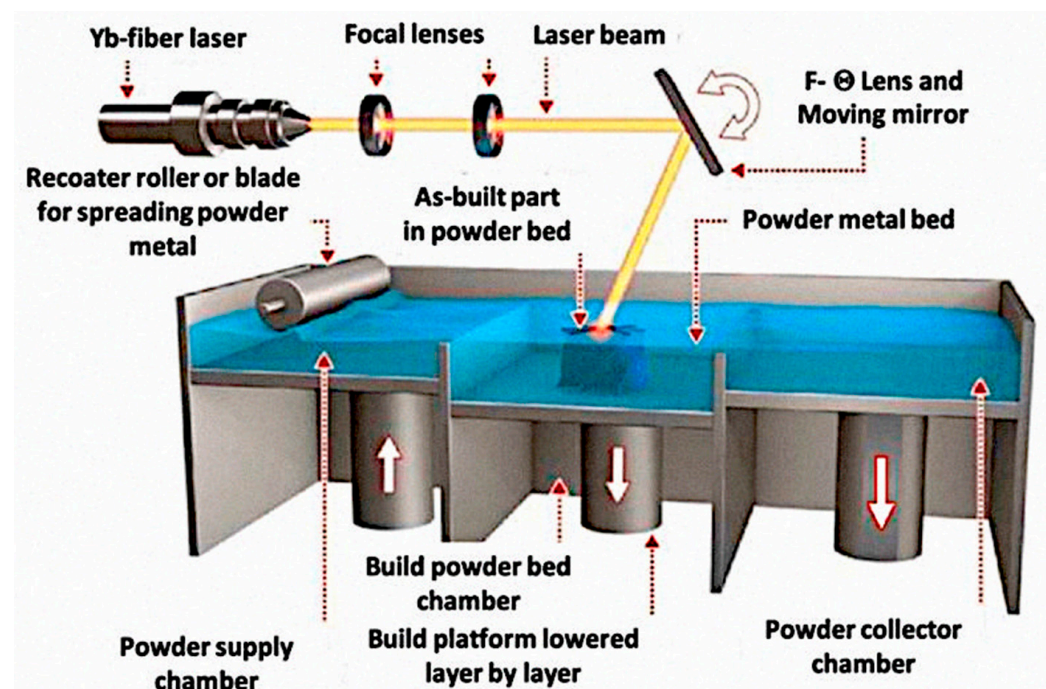


Figure 12. Schematic representation of the L-BPF process [51].

A direct energy deposition method was adopted by Liu et al. to investigate the printing capabilities of tungsten and tungsten alloys. A collimation of components for an X-ray telescope was the goal of this project [52]. To print the W-7Ni-3Fe alloys, Zhang and his colleagues used laser powder bed fusion [53]. In addition, Zhang et al. printed pure tungsten via laser powder bed fusion [54]. Laser power sources of 90 W and 170 W with polyhedral and spherical particles, respectively, were used to study the effect of relative density on scan speed and hatch spacing [55,56]. In a 90 W laser source sample, a 60–75% density was achieved. Figure 13 shows the relative density of 96.4–99.26% with cracks created by a 170 W laser source, in contrast. There was no correlation between scanning speed and relative density when the hatch spacing was kept constant. Even with a constant scanning speed, a reduction in hatch spacing from 30 to 15 microns [57] or 50 to 40 microns [58] improved relative density. Density was unaffected by hatch spacing increases more significant than 50 microns.

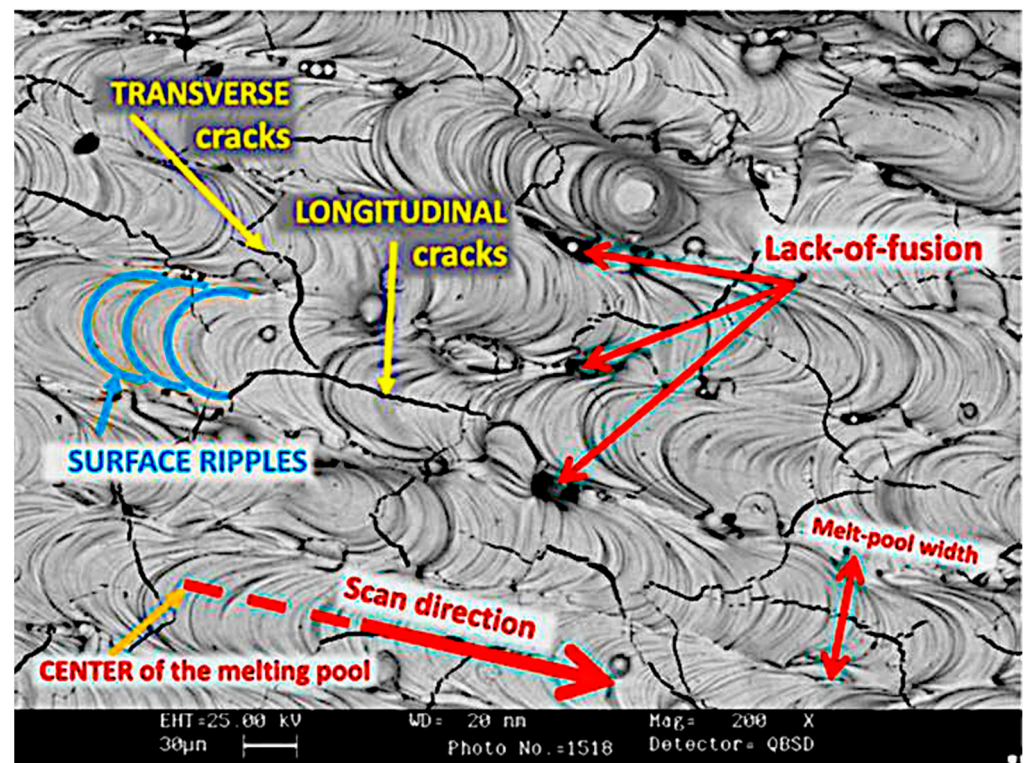


Figure 13. Crack on the tungsten surface in LPBF processed sample [58].

Typically, additive-manufactured components have defects such as keyholing, lack of fusion, and balling. Keyholing occurs when a high-power material is scanned at a low speed, causing pores to develop [59]. Inversely, a lack of fusion occurs when the input energy is insufficient. Gaps in printed pieces may also indicate balling defects. Zhang et al. used a plate-to-bottom distance measurement to determine the change in hardness in manufactured samples. A decrease in hardness was found as the distance increased. For example, the hardness of the W-10Ni alloy dropped from 490 to 250 HV in the L-PBF processed samples, whereas the hardness of the W-40Ni alloy dropped from 810 to 300 HV. With an increase in valence electron density, WHA alloys show a hardness increase of 360–395 HV [60,61].

On the other hand, the hardness of the W-7Ni-3Fe alloy decreased when the L-PBF sample was heat treated, according to Ivekovic et al. During the heat treatment, the spheroidization of tungsten may have occurred. Additively created W-Cr alloy had a two times more refined microstructure than conventionally sintered parts in a study by Bose et al. that assessed the hardness of conventionally sintered W-Cr alloy. According to Yan et al.'s research, the hardness decreases with increasing Ni concentration in W-Ni and W-Ni-Cu alloys [62]. The melting pool temperature increases due to the growth of small grains. In addition, the hardness of Y_2O_3 particles increases with the reduction in grain size from micron to nanoscale [63]. Some papers published the numerical value of Vickers microhardness for W-based powder composites. BMD's W-Cr component was found to have a maximum hardness of 966 HV in these studies. Due to the greater ductile-to-brittle transition temperature and the higher solidification rate, printing tungsten parts free of cracks is problematic in the AM process. At the same time, finer particles with lower oxygen content in the manufacturing cavity could lessen the density of cracks during fabrication.

3. Sintering Kinetics of Tungsten-Heavy Alloys

A series of microstructure formation stages are involved in the WHA consolidation process utilizing LPS. Several necklines exist between powder particles in the first stage of solid-phase sintering. The liquid then wets the solid tungsten grains, causing a rapid

rearrangement of the particles. The capillary force generated by the liquid wetting aids in reorganizing the tungsten granules. The liquid then enters and reorganizes loosely packed particle clusters [64,65]. Because the transitional elements are soluble in tungsten, the liquid dissolves some of the metal and then precipitates on bigger tungsten grains during the intermediate step of solution–reprecipitation. This stage sees significant grain shape accommodation and pore reduction. Net surface energy is reduced due to simultaneous liquid fills and the elimination of pores. Microstructural coarsening and very little densification occur in the final stage of the process [66]. The final stage's objective is to lower the surface energy. The solution–reprecipitation process continues in this step, followed by the coalescence of grains. Grain expansion is mediated mainly by gain coalescence [67]. Figure 14 depicts the grain growth in different stages during sintering process.

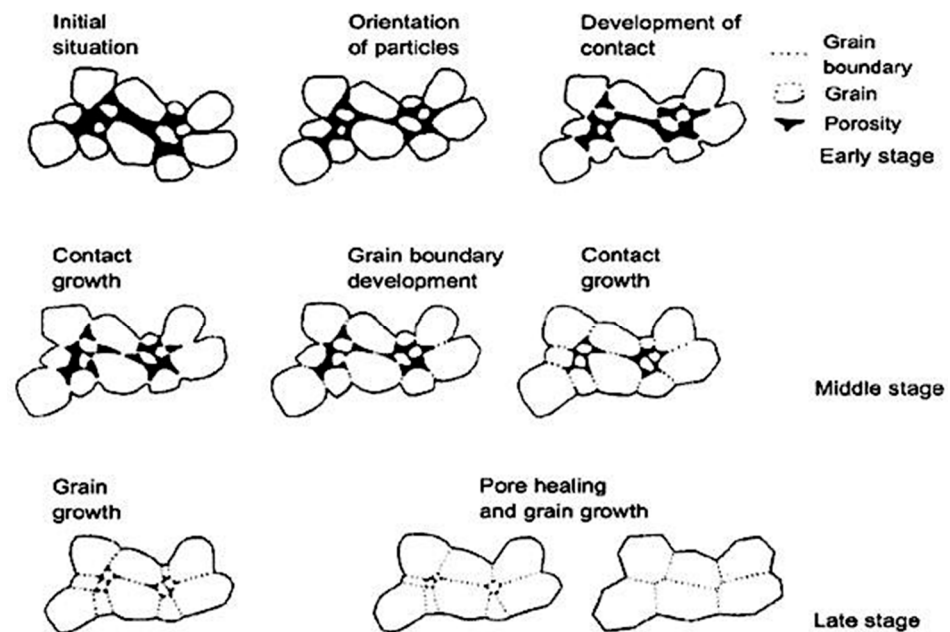


Figure 14. Grain growth during the sintering process. (Source: http://www.keramverband.de/brevier_engl/4/1/4_1_4.htm, accessed on 15 September 2022) [68].

The coarsening of grains during sintering can be expressed as $G^n(t) - G^n(o) = kt$ in the LPS process. $G(o)$ is the grain size at the beginning stage, $G(t)$ is the final grain size at a constant temperature with time t , and K is the grain growth rate [69]. The grain growth might vary with distinct diffusion models during sintering. Metal and non-metal particle sintering can be described using several diffusion models [70,71]. Cold compacts are typically heated between the significant constituent element's 0.5–0.7 melting temperature. Particles in a compressed state are held together by a mass transfer mechanism. Diffusional processes depend on a reduction in surface energy as a primary driving force. This suggests that tungsten compaction at temperatures between 1300 °C and 1750 °C is most likely regulated by grain boundary diffusion because of the higher diffusion coefficients and lower sintering activation energy [72]. According to a study by Jianxin Liu, grain rearrangement can be improved by enhancing capillary activity. In addition, it is evident that based on experimental and theoretical data, the grain arrangement factor increases with dihedral angle and volume percentage in the solid phase [73].

On the other hand, Grain coalescence affects grain growth formation, which was found in Makarova's metallographic studies. Moreover, a low melting point, solubility in both solid and liquid, and wettability are all shown to affect the sintering process in this research [74]. During sintering, the rate of bulk change is related to changes in diffusion coefficients, as described by Kothari. This investigation carried out the sintering of 3-micron tungsten powder at 1000–1500 °C. As a result, grain boundary diffusion control was ob-

served. The processing environment imposed by the technique is critical in describing WHAs properties. Powders were treated with hydrogen to remove oxides. Embrittlement in hydrogen, on the other hand, is possible. When embrittlement occurs in powders, vacuum sintering can be employed to remove it and improve the alloy's ductility. This is due to the contaminants being isolated at the grain boundaries of the W-matrix [75]. Therefore, combined environments during sintering might have the potential for higher results. In the beginning, dry and wet hydrogen and nitrogen atmospheres were used in the subsequent and final stages to achieve the best results [76]. Tungsten grains are separated from the matrix microstructure by a unique microstructure of pure tungsten [77–79]. A binder's tensile strength and ductility are directly related to the contiguity and connectivity of the tungsten in the binder. The ultimate tensile stress is highest at a volume percentage of 0.85 W in the WHAs and then drops as the volume fraction lowers. Connectivity between the tungsten–tungsten and tungsten–binder alter the mode of fracture. With increasing tungsten content, the ability to elongate a material decrease, which leads to a brittle mode of fracture due to higher contiguity [80,81]. Compositions and processing variables can alter the properties of WHAs. The properties of WHAs were studied by a number of researchers who looked at the effect of matrix binder compositions (Ni:Fe or Ni:Cu). Compositions based on either 7Ni:3Fe or 8Ni–2Fe ratios have shown the best combination of attributes [82–84]. Liquid-phase sintering of tungsten-heavy alloys is affected by measurable gravity because of the high alloy density and large solid–liquid density difference. The density difference between the liquid matrix and the solid particles is about 9 g/cm³, which causes the pores to rise owing to buoyancy and solid particles to settle, resulting in a measurable pore and solid gradient. It is important to manipulate the sintering microstructure to induce distortion-free densification. To avoid the shape distortion effect during sintering, the amount of matrix liquid fraction should be maintained between 18–35% of total volume of compact. As binder content decreases, the density of system might decrease, which results in shape distortion during sintering. In order to improve the DBTT of tungsten at low temperature, alloying additions were employed; as tungsten decreases below 88 wt.% it is not suitable for heavy dense applications.

3.1. Manufacturing of W–Ni–Cu WHA

The first binder proposed for the LPS sintering of WHA was Ni–Cu. They discovered that the ideal composition depends on the sintering process's temperature and time [85]. Furthermore, density difference over 9 g/cc between binder and tungsten creates tungsten grains settling in the gravity direction, leading to shape distortions during sintering. The densification of alloys is significantly altered by the presence of liquids, which account for about 25% of the total volume [86]. Ni to Cu is typically 3:2 to 4:1. The isomorphous system comprises Ni and Cu. Copper is completely soluble in nickel, whereas tungsten is not [87]. The Cu–Ni binary phase diagram shows that solidus temperatures fall between Cu and Ni's fusion points. In W–Ni–Cu heavy alloy combination, tungsten solubility in matrix dramatically reduced solidus and liquidus temperatures. Price et al. focused on the effects of composition using an 80–97 wt.% of W with remaining Ni–Cu alloy's properties. Due to tungsten's insoluble nature with copper, when the two metals were mixed, the pure W particles became moist and bonded together. As a result, there was no evidence of grain development, leading to increased porosity. At a temperature of 1600 °C, nickel added to W resulted in virtually complete density. When copper and nickel are combined, the binder matrix (Ni:Cu) ratio plays a crucial role in densification, as does tungsten. When 89–93 percent W and a Ni:Cu ratio of 2:1 were combined, higher densities could be achieved. During the sintering process, the mean grain size of tungsten grows as the binder matrix increases in W–Cu–Ni-heavy alloys [88]. German et al. addressed the numerical analysis of W–Ni–Cu. Because adequate sintering time results in an increase in the average grain size; at the beginning of LPS, the contiguity and connectivity of W decrease. These changes indicate that solids have been broken down into smaller pieces. Microstructural properties in different samples were shown to be unaffected by gravitational orientation [89]. Four

other tungsten-heavy alloys were studied by Jiten das et al. They discovered that low W and a stable Ni:Cu ratio had better hardness and tensile strength. Tests on these alloys found that they failed most frequently at the interface. The tungsten grain size was found to impact the failure mode as shown in Figure 15 [90]. Figure 16 shows that contact failure occurred when larger tungsten grains were present. The fracture mechanism gradually changes from interface failure to grain cleavage failure as the grain size decreases.

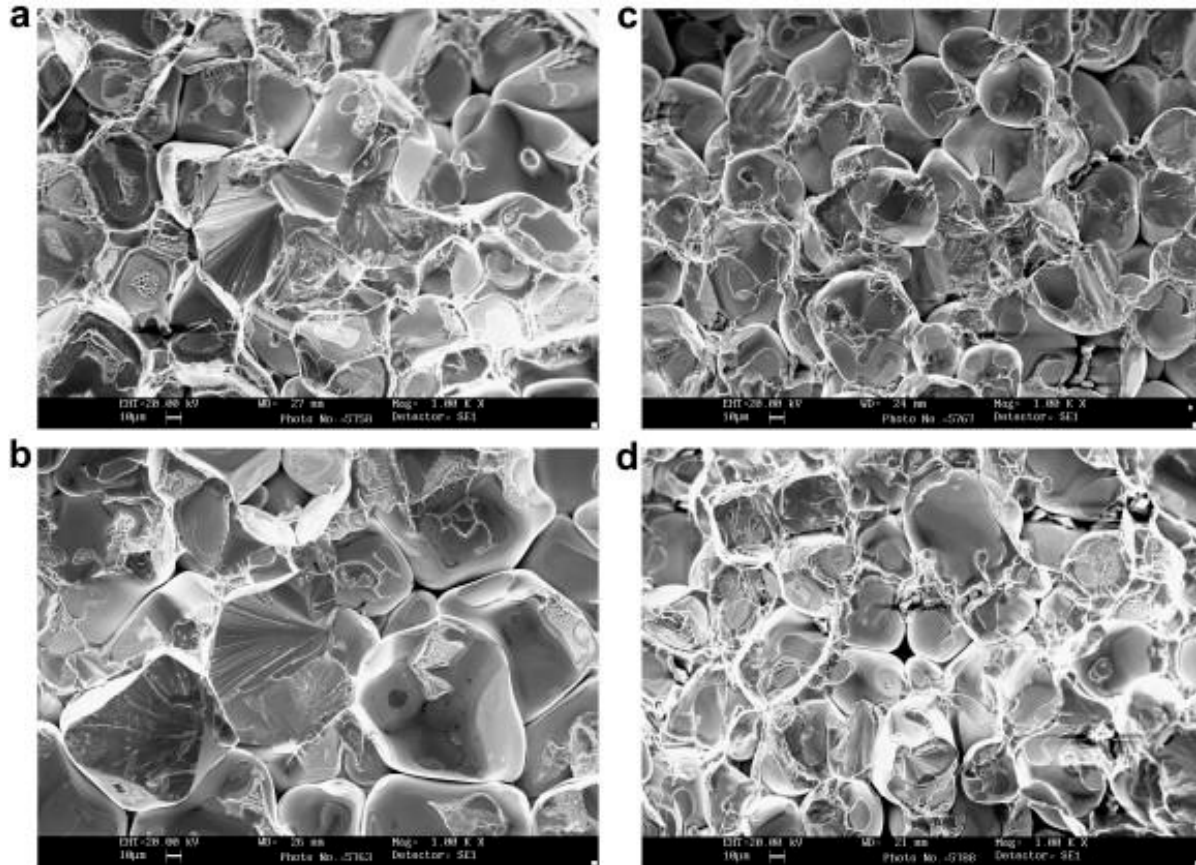


Figure 15. SEM fractography images of W-Ni-Cu-heavy alloy [90]. (a) W-94.9, Ni-3.4, Cu-1.7 alloy, (b) W-96.1, Ni-2.8, Cu-1.1 alloy, (c) W-92.5, Ni-5, Cu-2.5 alloy and (d) W-96.0, Ni-2.8, Cu-1.1, Fe-0.1 alloy.

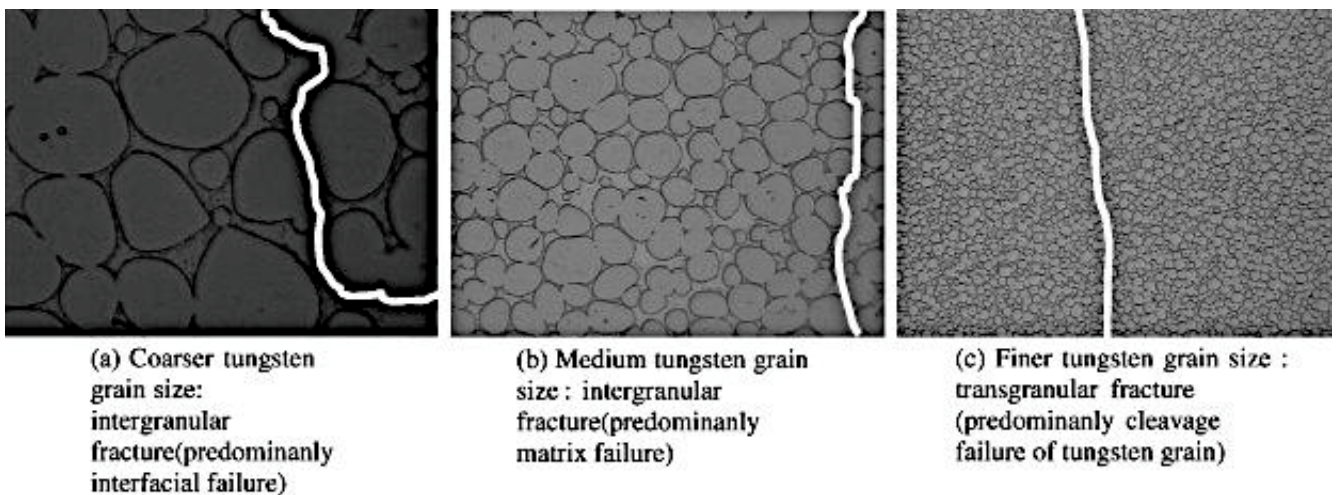


Figure 16. Schematic representation of fracture in W-heavy alloy [90].

Matrix failure is more common in alloys with medium grain sizes, as has been discovered. Cleavage fracture is the most common failure mode when the W grain size is smaller. The release of interfacial energy has been high because of the small grain sizes of the tungsten and binder in the new interface development. A straight line (transgranular) rupture of the tungsten particle occurs (refer. Figure 16c). As a result, intergranular fractures would occur at bigger grain sizes. Because of the following, this may be the case. An intergranular fracture requires less energy to propagate a crack than a transgranular mode. There are fewer twists in the intergranular fracture propagation path with larger tungsten grains. The energy transfer between the binder matrix and the W particle is lower for bigger tungsten grains than for smaller ones. The tungsten particle will not be fragmented in medium-sized grains because the fracture path tortuosity and the interfacial energy are not high enough. As a result, cracks in the medium W grains propagate perpendicular to the matrix.

3.2. Manufacturing of W–Ni–Mn WHA

With its low thermal conductivity and melting temperature, manganese has the potential to promote the adiabatic shear band. Low heat dissipation in the localized region of the material and unstable strain in the interior section of the material are the two causes of shear band development. As a result, limited thermal conduction, strain hardening rates, and thermal softening are likely to favour adiabatic shear [91]. Based on this premise, tungsten with a (Ni:Mn) matrix may be prone to adiabatic shear production. Thermal conductivity, hardness, and microscopic grains of W in the alloy all have a role in creating adiabatic shear bands (ASB) [92,93]. It was also demonstrated by Bose and German et al. that the manganese element added to tungsten-heavy alloys increases ASB [94–96]. Tungsten-heavy alloy densification incorporates particle size, compaction pressure, temperature, and environment. Densification is limited by oxygen, which can be found in the powder [97]. Oxygen in metal has a significant impact on alloy mechanical characteristics. To avoid manganese oxidation and vapor pressure during compaction, it is, therefore, crucial to select an optimal Ni:Mn ratio [98]. On the other hand, Manganese has a significant oxidation risk because of its oxygen content, making it challenging to densify and hence decreasing the performance of W–Ni–Mn-heavy alloys. It is possible that a vacuum sintering atmosphere could be used as a solution to the problems stated above. SPS sintering of the W–Ni–Mn-heavy alloy was studied by Pan et al. Thus, they were able to produce W–Ni–Mn-heavy alloy with a fine grain microstructure utilizing SPS. Despite this, SPS cannot be used in large-scale production because of the high cost of the necessary equipment. There is a need to create a new sintering process for these alloys as an alternative to SPS. Using a vacuum atmosphere during sintering will effectively eliminate oxygen from the metal [99,100]. The mechanical properties of the alloy are greatly influenced by factors such as connectivity, contiguity, and sintered relative density. The production of MnO in the alloy during the sintering process has previously been shown to inhibit the alloy's densification [101]. There was, however, only a cursory examination of the effects of sintering oxygen in depth.

3.3. Manufacturing of W–Ni–Fe WHA

The solubility of tungsten dictates the distribution of W in a tungsten-heavy alloy's binder matrix. For W–Ni–Fe-heavy alloy, the solubility of W in the binder is 16 wt.%. The melt fills the pores as it flows across the grain boundaries. Densification is also induced by filling in the neck of particles, decreasing the contact surface energy. Fe–Ni phase diagrams show that nickel and iron can be solubilized at temperatures ranging from 800 to 1500 °C. In W–Ni–Fe-heavy alloy, the liquid phase is formed at 1465 °C [102]. Liu et al. used conventional SPS to examine the microstructure of a 93W–5.6Ni–1.4Fe alloy that had been sintered. Several trials with varying heating rates (between 100 and 380 degrees Celsius per minute) revealed the sintering temperature. Traditional methods employed a compaction pressure of 250 MPa. Traditional SPS yielded a relative density of 98.5 percent and 95 percent, respectively. As a result, the SPS-treated sample has less weight because of its reduced sintering time. The liquid phase solution–reprecipitation mechanism is therefore

regulated [103,104]. In a study by Changsheng et al., multiple heating rates (20–105 °C/min) were utilized in a 90W–7Ni–3Fe-heavy alloy, and the results were published. The sintering was performed for 10 min using the microwave, 30 min using the conventional method, and 1480 °C, respectively. Heat rate effects in a 90W–7Ni–3Fe-heavy alloy are shown in Table 3.

80 °C/min offers higher mechanical properties among the various heating rates used in this technique. A minor amount of tungsten was also found to develop at a quicker heating rate [105]. When a penetrator fails, the creation of shear bands is critical. In dynamic mode, Ramesh et al. observed shearing deformations in WHA. Shear deformations reveal a 25% decrease in the area. Figure 17 depicts the tensile test's effect on the shear band. Several tensile cracks were formed at a 45-degree angle to the shearing direction. Compounds have no vacuum expansion or fracture formation in the rich matrix. However, the shear strain rate for the torsion test was 10% at shear localization [106].

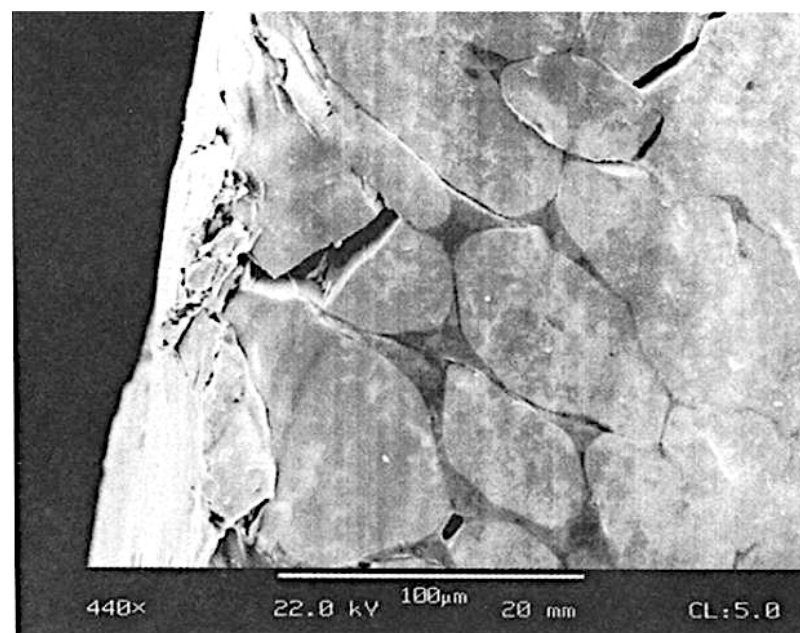


Figure 17. Microcracks at W-W grain boundaries in shear band region [106].

It is projected that the ASB (adiabatic shear bands) will rise in a narrow region when tungsten alloys replace depleted uranium (DU) alloys in defence applications [107]. The ASB is partly maintained by characteristics such as continuity and connection within the tungsten and binder matrix. The compact may be distorted if the liquid phase has volume fractions more significant than 35%. An increase in density of more than 9 g/cc may cause the compact to shape deform. As a result, the alloy retains a 20% liquid volume [108]. The 80W–14Ni–6Fe alloy was shown to have a distortion in its behaviour by German et al. A relative density of 74% was achieved when the compact was sintering at 1475 °C. It suggests that solid phase sintering has a low densification rate. When temperatures rise above 1475 °C, the liquid phase begins. As a result, there were no substantial changes in densities. However, sintering at 1500 °C resulted in practically complete densification. At this temperature, the sintering time was increased to 30 min to observe how distortion occurs. A lot of distortion could be seen at this stage. As a result of the alloy's deformation and microstructural changes, the relative density of the compact may have decreased [109].

Mondal et al. [37] examined the sintering behaviour of 90W–7Ni–3Fe alloy in conventional and microwave sintering modes and measured shrinkage in the compaction process in axial and radial directions. Microwave samples shrank more than traditional samples. Pore curvature differences lead to an uneven dimensional shift. Shrinkage rates in microwave-sintered samples change dramatically, as seen in Figure 18 [110].

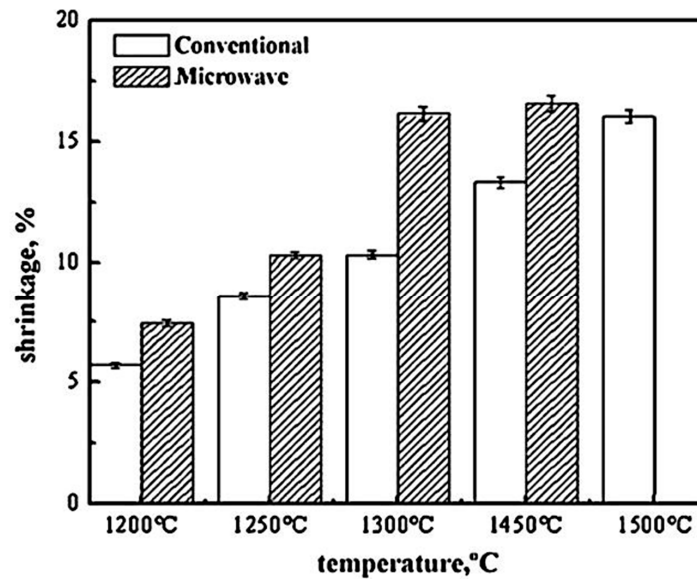


Figure 18. The heating mode impacts radial shrinkage [110].

The conventionally sintered alloy has lower hardness and fracture strength than microwave sintered parts. Because of the spherical shape of the tungsten in the microwave-sintered component, crack propagation may be limited due to less stress concentration factor [111]. Chemical and mechanical alloying procedures were used by Zeinab et al. to produce WHA. Significant densification was achieved for each sample generated by either method. The grain sizes of the milled powders typically range from 63 to 72 nm. The mechanical process produced larger granules than the chemical method. For alloys with small grain sizes, the chemical method works quite well. When conducting an electrical test, it is found that the mechanical alloyed portion has a higher electrical resistance than the chemically treated part. Fine-grained alloys with decreased resistivity have higher free electron mobility, as seen in Figure 19 [112].

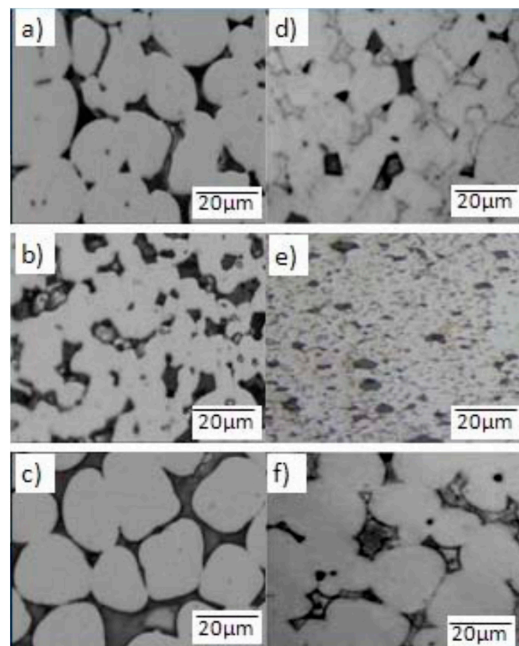


Figure 19. Optical image of WHA's (a) MA (95W-1.5Fe-3.5Ni), (b) MA (93W-1Fe-4.5Ni-1.5Co), (c) MA (90W-4Cu-6Ni), (d) chemical method (95W-1.5Fe-3.5Ni), (e) chemical method (93W-4.5Ni-1Fe-1.5Co), (f) chemical method (90W-4Cu-6Ni).

According to Hwang et al., polyhedral particles have greater activation energies than non-polyhedral particles. The sintered part microstructure has a finer grain size in the chemically processed part than in the mechanically processed part [113]. The tensile characteristics of the WHA (90W–7Ni–3Fe, 90W–6Ni–2Fe–2Co) sintered by conventional microwave sintering at 1460 °C and 1470 °C, respectively, were studied by Prabhu et al. [36]. The microwave and regular sintered parts both had transgranular and intergranular fracture modes. Figure 20 depicts a variety of fracture modes: intergranular fracture mode is indicated by points 1 and 4, respectively [114].

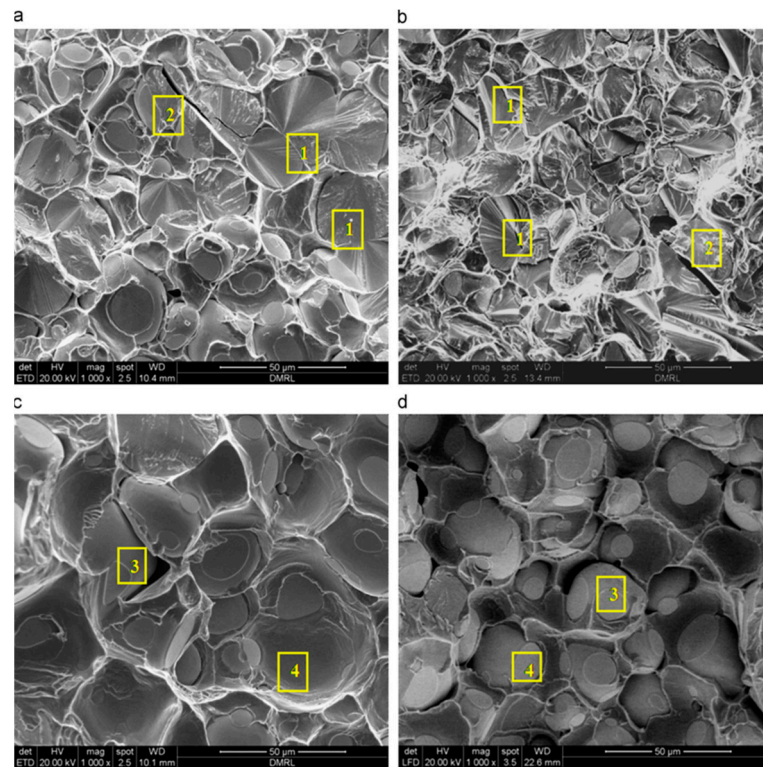


Figure 20. Fractography images (a) 90W–3Fe–7Ni (MW-sintered), (b) 90W–2Fe–6Ni–2Co (MW-sintered), (c) 90W–3Fe–7Ni (conventionally sintered), (d) 90W–2Fe–6Ni–2Co (conventionally sintered).

It was found that the SPS process yields tungsten grains with a finer grain size than traditional sintering, according to Li and colleagues. Conventional sintering results in coarser grains because of the lengthy processing time [115]. On the other hand, industrial potential of SPS production rate is low even at higher production speeds for samples with diameters in the range of 15–50 mm, for which it is easy to achieve uniform heating of the sample. However, if the sample diameter is in the range of 100–300 mm, a significant temperature gradient inside the sample may occur which results in nonuniform densification. The necessity of very high current to achieve very high temperatures and high heating rates has significant implications towards the efficiency of SPS. The various mechanisms contribute differently at different stages of sintering. Identification of the contribution of each mechanism will enable us to design more practicable and efficient processing techniques in the future [116].

4. Conclusions

Microwave sintering has the potential to produce finer microstructures with superior mechanical characteristics than conventional sintering. As a result, the microwave sintering diffusion rate will increase, contributing to better material densification.

A maximum heating rate of 10 °C/min can be achieved in the conventional mode, while a maximum of 400 °C/min can be completed in the microwave mode. Microwave sintering has a better chance of achieving higher densification than conventional sintering.

The microwave sintering method used less electrical energy than the conventional method. Using microwave sintering, the densification time is shortened by around 90%. For this reason, microwave sintering of WHA is commonly employed.

SPS can be completed within 20 min. In this way, the grain growth rate is limited during the operation, allowing alloys to achieve more significant densification. Optimizing process parameters such as pressure, temperature, and heating rate could lead to a relative density above 97%.

Additive manufactured pure tungsten has a hardness value of 474 HV, comparable hardness value of conventionally manufactured parts.

AM-created W–Cr composites have a density of 98% and a hardness of 966 HV. It demonstrates that additive manufacturing may print tungsten with diverse alloying components.

Particle size can have a significant impact on the mechanical properties of sintered parts, and it is clear that smaller particles do not always provide higher densification. Powder morphology and other properties, such as flowability, affect these outcomes. Additional elements like tantalum, molybdenum, and rhenium may help WHA perform better in particular applications.

Author Contributions: Conceptualization, R.M. and A.R.A.; methodology, R.M. and A.R.A.; investigation, A.R.A.; writing—original draft preparation, R.M. and A.R.A.; writing—review and editing, R.M. and A.R.A.; supervision, A.R.A. All authors have read and agreed to the published version of the manuscript.

Funding: This research received no external funding.

Data Availability Statement: Not applicable.

Conflicts of Interest: The authors declare no conflict of interest.

References

1. Lide, D.R. (Ed.) *CRC Handbook of Chemistry and Physics*; Internet Version 2005; CRC Press: Boca Raton, FL, USA, 2005. Available online: <http://www.hbcpnetbase.com> (accessed on 28 September 2022).
2. Brink, A. A Guide to the Elements. *Crystallogr. Rev.* **2019**, *25*, 157–159. [[CrossRef](#)]
3. Gaur, R.P.S. Modern Hydrometallurgical Production Methods for Tungsten. *JOM* **2006**, *58*, 45–49. [[CrossRef](#)]
4. Savitskii, E.M. Properties of tungsten-rhenium alloys. *Met. Sci. Heat Treat. Met.* **1960**, *2*, 483–486. [[CrossRef](#)]
5. Ren, C.; Fang, Z.Z.; Koopman, M.; Butler, B.; Paramore, J.; Middlemas, S. Methods for improving ductility of tungsten—A review. *Int. J. Refract. Met. Hard Mater.* **2018**, *75*, 170–183. [[CrossRef](#)]
6. Tan, Z.Y.; Wu, X.; Zhu, W.; Guo, J.W.; Wang, W.; Ma, Z.S. Ultra-high hardness induced by W precipitation within Ta-Hf-W-C ultra-high temperature ceramic coatings. *J. Eur. Ceram. Soc.* **2022**, *42*, 6288–6294. [[CrossRef](#)]
7. Bhattarai, J.; Akiyama, E.; Habazaki, H.; Kawashima, A.; Asami, K.; Hashimoto, K. The passivation behavior of sputter-deposited W-Ta alloys in 12M HCl. *Corros. Sci.* **1998**, *40*, 757–779. [[CrossRef](#)]
8. Wu, Y. Research Progress in Irradiation Damage Behavior of Tungsten and Its Alloys for Nuclear Fusion Reactor. *Jinshu Xuebao Acta Metall. Sin.* **2019**, *55*, 939–950. [[CrossRef](#)]
9. Wang, S.; Luo, L.M.; Shi, J.; Zan, X.; Zhu, X.Y.; Luo, G.N.; Wu, Y.C. Effect of mechanical alloying on the microstructure and properties of W–Ti alloys fabricated by spark plasma sintering. *Powder Technol.* **2016**, *302*, 1–7. [[CrossRef](#)]
10. Amalu, N.I.; Okorie, B.A.; Ugwuoke, J.C.; Obayi, C.S. Electrical Conductivity of Spark Plasma Sintered W-Cu and Mo-Cu Composites for Electrical Contact Applications. *J. Miner. Mater. Charact. Eng.* **2021**, *9*, 48–60. [[CrossRef](#)]
11. Meng, Y.; Zhang, J.; Duan, C.; Chen, C.; Feng, X.; Shen, Y. Microstructures and properties of W-Cu functionally graded composite coatings on copper substrate via high-energy mechanical alloying method. *Adv. Powder Technol.* **2015**, *26*, 392–400. [[CrossRef](#)]
12. Leung, C.H.; Wingert, P.C. Microstructure Effects on Dynamic Welding of Ag/W Contacts. *IEEE Trans. Common. Hybrids Manuf. Technol.* **1988**, *11*, 64–67. [[CrossRef](#)]
13. Upadhyaya, A. Processing strategy for consolidating tungsten heavy alloys for ordnance applications. *Mater. Chem. Phys.* **2001**, *67*, 101–110. [[CrossRef](#)]
14. Wurster, S.; Baluc, N.; Battabyal, M.; Crosby, T.; Du, J.; García-Rosales, C.; Hasegawa, A.; Hoffmann, A.; Kimura, A.; Kurishita, H.; et al. Recent progress in R&D on tungsten alloys for divertor structural and plasma facing materials. *J. Nucl. Mater.* **2013**, *442*, 181–189. [[CrossRef](#)]

15. Handtrack, D.; Tabernig, B.; Kestler, H.; Pohl, P.; Glatz, W. Tungsten Heavy Alloys for Collimators and Shielding in the X-ray Diagnostics. In Proceedings of the 18th Plansee Seminar, Reutte, Austria, 3–7 June 2013; pp. 1–9.
16. Lee, Y.H.; Choi, C.H.; Jang, Y.T.; Kim, E.K.; Ju, B.K.; Min, N.K.; Ahn, J.H. Tungsten nanowires and their field electron emission properties. *Appl. Phys. Lett.* **2002**, *81*, 745–747. [[CrossRef](#)]
17. Price, G.H.S.; Smithells, C.J.; Williams, S.V. Sintered alloys. Part I. Copper-nickel-tungsten alloys sintered with a liquid phase present. *J. Inst. Met.* **1938**, *62*, 239–264.
18. Bryant, C.L.; Bewley, B.P. *The Coolidge Process for Making Tungsten Ductile: The Foundation of Incandescent Lighting*; Cambridge University Press: Cambridge, UK, 1910; pp. 67–73.
19. Lassner, E.; Schubert, W.-D. *Properties, Chemistry, Technology of the Element, Alloys, and Chemical Compounds*; Vienna University of Technology: Vienna, Austria, 1999; pp. 124–125.
20. Upadhyaya, G.S. *Powder Metallurgy Technology*; Cambridge International Science Publishing: Cambridge, UK, 2014.
21. Majumdar, S.; Kishor, J. Demonstration of Production of Tungsten Metal Powder and its Consolidation into Shapes. *BARC Newsl.* **2016**, 30–33.
22. Popov, O.; Vishnyakov, V. High Densification of Tungsten via Hot Pressing at 1300 °C in Carbon Presence. *Materials* **2022**, *15*, 3641. [[CrossRef](#)]
23. Andreja, Š.; Jenu, P.; Zava, J.; Mirin, Č. Materials Characterization The role of tungsten phases formation during tungsten metal powder consolidation by FAST: Implications for high-temperature applications. *Mater. Charact.* **2018**, *138*, 308–314. [[CrossRef](#)]
24. Karpinos, D.M.; Kravchenko, A.A.; Pilipovskii, Y.L.; Tkachenko, V.G.; Shamatov, Y.M. Reaction of tungsten with die material in hot pressing. *Sov. Powder Metall. Met. Ceram.* **1970**, *9*, 831–834. [[CrossRef](#)]
25. McCarty, L.V.; Donelson, R.; Hehemann, R. A diffusion model for tungsten powder carburization. *Met. Mater. Trans. A* **1991**, *18*, 969–974. [[CrossRef](#)]
26. Jiang, Y.; Yang, J.F.; Zhuang, Z.; Liu, R.; Zhou, Y.; Wang, X.P.; Fang, Q.F. Characterization and properties of tungsten carbide coatings fabricated by SPS technique. *J. Nucl. Mater.* **2013**, *433*, 449–454. [[CrossRef](#)]
27. Juenke, E.F. Refractory Transition Metal Compounds; High-Temperature Cermets. *Nucl. Sci. Eng.* **1966**, *24*, 420–421. [[CrossRef](#)]
28. Gómez, A.J. *UC San Diego San Diego Electronic Theses and Dissertations*; UC San Diego: La Jolla, CA, USA, 2010.
29. Stephens, J.R. *Effects of Interstitial Impurities on the Low-Temperature Tensile Properties of Tungsten*; National Aeronautics and Space Administration: Washington, DC, USA, 1964.
30. *ASM Handbook*, 9th ed.; ASM International: Materials Park, OH, USA, 1993; Volume 7, pp. 389–390.
31. Poster, A.R. Factors Affecting the Compaction of Tungsten Powders. *Powder Met.* **1962**, *5*, 301–315. [[CrossRef](#)]
32. Sharma, A.K.; Gupta, S. Microwave Processing of Biomaterials for Orthopaedic Implants: Challenges Microwave Processing of Biomaterials for Orthopaedic Implants: Challenges and Possibilities. *JOM* **2020**, *72*, 1211–1228. [[CrossRef](#)]
33. Agrawal, D. *Microwave Sintering of Ceramics, Composites Metal Powders*; Woodhead Publishing Limited: Sawston, UK, 2010. [[CrossRef](#)]
34. Roy, R.; Agrawal, D.; Cheng, J. Full sintering of powdered-metal bodies in a microwave sintering of powdered-metal bodies. *Nature* **1999**, *401*, 304. [[CrossRef](#)]
35. Jain, M.; Kandan, G.; Martin, K.; Kapoor, D.; Cho, K.; Klotz, B.; Dowding, R.; Agrawal, D.; Cheng, J. Microwave sintering: A new approach to fine-grain tungsten—II. *Int. J. Powder Metall.* **2006**, *42*, 53–57.
36. Prabhu, G.; Chakraborty, A.; Sarma, B. Microwave sintering of tungsten. *Int. J. Refract. Met. Hard Mater.* **2009**, *27*, 545–548. [[CrossRef](#)]
37. Mondal, A.; Upadhyaya, A.; Agrawal, D. Effect of heating mode on sintering of tungsten. *Int. J. Refract. Met. Hard Mater.* **2010**, *28*, 597–600. [[CrossRef](#)]
38. Wang, K.; Wang, X.P.; Liu, R.; Hao, T.; Zhang, T.; Liu, C.S.; Fang, Q.F. The study on the microwave sintering of tungsten at relatively low temperature. *J. Nucl. Mater.* **2012**, *431*, 206–211. [[CrossRef](#)]
39. Hu, Z.Y.; Zhang, Z.H.; Cheng, X.W.; Wang, F.C.; Zhang, Y.F.; Li, S.L. A review of multi-physical fields induced phenomena and effects in spark plasma sintering: Fundamentals and applications. *Mater. Des.* **2020**, *191*, 108662. [[CrossRef](#)]
40. Tokita, M. Development of large-size ceramic/metal bulk FGM fabricated by spark plasma sintering. *Mater. Sci. Forum.* **1999**, *308–311*, 83–88. [[CrossRef](#)]
41. Tiwari, D.; Basu, B.; Biswas, K. Simulation of thermal and electric field evolution during spark plasma sintering. *Ceram. Int.* **2009**, *35*, 699–708. [[CrossRef](#)]
42. Olevsky, E.A.; Kandukuri, S.; Froyen, L. Consolidation enhancement in spark-plasma sintering: Impact of high heating rates. *J. Appl. Phys.* **2007**, *102*, 114913. [[CrossRef](#)]
43. Olevsky, E.A.; Froyen, L. Impact of thermal diffusion on densification during SPS. *J. Am. Ceram. Soc.* **2009**, *92*, 122–132. [[CrossRef](#)]
44. Gao, Z.; Viola, G.; Milsom, B.E.N.; Whitaker, I.; Yan, H.; Reece, M.J. Kinetics of Densification and Grain Growth of Pure Tungsten During Spark Kinetics of Densification and Grain Growth of Pure Tungsten During Spark Plasma Sintering. *Met. Mater. Trans. A* **2012**, *43*, 1608–1614. [[CrossRef](#)]
45. Villenova, M.; Nerval, B.; Pala, Z.; Janata, M.; Tonarová, D. Properties of Ultrafine-Grained Tungsten Prepared by Ball Milling and Spark Plasma Sintering. *Appl. Mech. Mater.* **2015**, *4*, 346–347.
46. Hu, K.; Li, X.-Q.; Yang, C.; Li, Y.-Y. Densification and microstructure evolution during SPS consolidation process in W-Ni-Fe system. *Trans. Nonferrous Met. Soc. China* **2011**, *21*, 493–501. [[CrossRef](#)]

47. Anselmi-Tamburini, U.; Gennari, S.; Gary, J.E.; Munir, Z.A. Fundamental investigations on the spark plasma sintering/synthesis process: II. Modelling current and temperature distributions. *Mater. Sci. Eng. A* **2005**, *394*, 139–148. [[CrossRef](#)]
48. Omole, S.; Lunt, A.; Kirk, S.; Shokrani, A. Advanced Processing and Machining of Tungsten and Its Alloys. *J. Manuf. Mater. Process.* **2022**, *6*, 15. [[CrossRef](#)]
49. Guo, M.; Gu, D.; Xi, L.; Du, L.; Zhang, H.; Zhang, J. Formation of scanning tracks during Selective Laser Melting (SLM) of pure tungsten powder: Morphology, geometric features and forming mechanisms. *Int. J. Refract. Metals Hard Mater.* **2019**, *79*, 37–46. [[CrossRef](#)]
50. Zhang, J.; Gu, D.; Yang, Y.; Zhang, H.; Chen, H.; Dai, D. Influence of Particle Size on Laser Absorption and Scanning Track Formation Mechanisms of Pure Tungsten Powder During Selective Laser Melting. *Engineering* **2019**, *5*, 736–745. [[CrossRef](#)]
51. Ozel, T.; Altay, A.; Kaftanoglu, B.; Leach, R.; Senin, N.; Donmez, A. Focus variation measurement and prediction of surface texture parameters using machine learning in laser powder bed fusion. *J. Manuf. Sci. Eng. Trans. ASME* **2019**, *142*, 1–26. [[CrossRef](#)]
52. Zhong, M.; Liu, W.; Ning, G.; Yang, L.; Chen, Y. Laser direct manufacturing of tungsten nickel collimation component. *J. Mater. Process. Technol.* **2004**, *147*, 167–173. [[CrossRef](#)]
53. Zhang, D.; Cai, Q.; Liu, J.; Li, R. Research on Process and Microstructure Formation of W-Ni-Fe Alloy Fabricated by Selective Laser Melting. *J. Mater. Eng. Perform.* **2010**, *20*, 1049–1054. [[CrossRef](#)]
54. Taylor, P.; Zhang, D.; Cai, Q.; Liu, J.; Zhang, D.; Cai, Q.; Liu, J. Materials and Manufacturing Processes Formation of Nanocrystalline Tungsten by Selective Laser Melting of Tungsten Powder Formation of Nanocrystalline Tungsten by Selective Laser Melting of Tungsten Powder. *Mater. Manuf. Process.* **2012**, *27*, 1267–1270. [[CrossRef](#)]
55. Enneti, R.K.; Morgan, R.; Atre, S.V. Effect of process parameters on the Selective Laser Melting (SLM) of tungsten. *Int. J. Refract. Met. Hard Mater.* **2018**, *71*, 315–319. [[CrossRef](#)]
56. Rebesan, P.; Bonesso, M.; Gennari, C.; Dima, R.; Pepato, A.; Vedani, M. Tungsten Fabricated by Laser Powder Bed Fusion. *BHM Berg- Hüttenmännische Mon.* **2021**, *166*, 263–269. [[CrossRef](#)]
57. Madison, J.D.; Alagesen, L.K. Quantitative characterization of porosity in laser welds of stainless steel. *Scr. Mater.* **2012**, *67*, 783–786. [[CrossRef](#)]
58. Zhang, D.Q.; Liu, Z.H.; Cai, Q.Z.; Liu, J.H.; Chua, C.K. Influence of Ni content on W–Ni alloy microstructure produced by selective laser melting. *Int. J. Refract. Metals Hard Mater.* **2014**, *45*, 15–22. [[CrossRef](#)]
59. Wang, M.; Li, R.; Yuan, T.; Chen, C.; Zhang, M.; Weng, Q. Selective laser melting of W-Ni-Cu composite powder: Densification, microstructure evolution and nano-crystalline formation. *Int. J. Refract. Metals Hard Mater.* **2018**, *70*, 9–18. [[CrossRef](#)]
60. Iveković, A.; Montero-Sistiaga, M.L.; Vanmeensel, K.; Kruth, J.P.; Vleugels, J. Effect of processing parameters on microstructure and properties of tungsten heavy alloys fabricated by SLM. *Int. J. Refract. Met. Hard Mater.* **2019**, *82*, 23–30. [[CrossRef](#)]
61. Bose, A.; Schuh, C.A.; Tobia, J.C.; Tuncer, N.; Mykulowycz, N.M.; Preston, A.; Barbati, A.C.; Kernan, B.; Gibson, M.A.; Krause, D.; et al. Traditional and additive manufacturing of a new Tungsten heavy alloy alternative. *Int. J. Refract. Metals Hard Mater.* **2018**, *73*, 22–28. [[CrossRef](#)]
62. Yan, A.; Wang, Z.; Yang, T.; Wang, Y.; Ma, Z. Microstructure, thermal physical property and surface morphology of W-Cu composite fabricated via selective laser melting. *JMADE* **2016**, *109*, 79–87. [[CrossRef](#)]
63. Hu, Z.; Zhao, Y.; Guan, K.; Wang, Z.; Ma, Z. Pure tungsten and oxide dispersion strengthened tungsten manufactured by selective laser melting: Microstructure and cracking mechanism. *Addit. Manuf.* **2020**, *36*, 101579. [[CrossRef](#)]
64. Mortensen, A. Kinetics of densification by solution-precipitation. *Acta Mater.* **1997**, *45*, 749–758. [[CrossRef](#)]
65. Johnson, J.L.; German, R.M. Solid-state contributions to densification during liquid-phase sintering. *Metall. Mater. Trans. B* **1996**, *27*, 901–909. [[CrossRef](#)]
66. Dowding, R.J. *The Recrystallization and Spheroidization of Tungsten Grains in a Tungsten-Heavy Alloy*; Army Materials Research Agency: Watertown, MA, USA, 1989.
67. Park, S.J.; Martin, J.M.; Guo, J.F.; Johnson, J.L.; German, R.M. Grain Growth Behaviour of Tungsten Heavy Alloys Based on the Master Sintering Curve Concept. *Met. Mater. Trans. A* **2006**, *37*, 3337–3346. [[CrossRef](#)]
68. Stages of Sintering. Available online: http://www.keramverband.de/brevier_engl/4/1/4_1_4.htm (accessed on 15 September 2022).
69. Kingery, W.D. Densification during Sintering in the Presence of a Liquid Phase. I. Theory. *J. Appl. Phys.* **1959**, *30*, 301–306. [[CrossRef](#)]
70. Coble, R.L. Sintering Crystalline Solids. II. Experimental Test of Diffusion Models in Powder Compacts. *J. Appl. Phys.* **1961**, *32*, 793–798. [[CrossRef](#)]
71. Vasilos, T.; Smith, J.T. Diffusion Mechanism for Tungsten Sintering Kinetics. *J. Appl. Phys.* **1964**, *35*, 215–218. [[CrossRef](#)]
72. German, R.M. *Liquid Phase Sintering Book*; Springer: New York, NY, USA, 1985. [[CrossRef](#)]
73. Liu, J.; German, R.M. Rearrangement densification in liquid-phase sintering. *Metall. Mater. Trans. A Phys. Metall. Mater. Sci.* **2001**, *32*, 3125–3131. [[CrossRef](#)]
74. Makarova, R.V.; Todorovich, O.K.; Frantsevich, I.N. The coalescence phenomenon in liquid-phase sintering in the systems tungsten-nickel-iron and tungsten-nickel-copper. *Sov. Powder Metall. Met. Ceram.* **1965**, *4*, 554–559. [[CrossRef](#)]
75. Kothari, N.C. Densification and grain growth during liquid-phase sintering of tungsten-nickel-copper alloys. *J. Less-Common. Met.* **1967**, *13*, 457–468. [[CrossRef](#)]
76. Bose, A.; German, R.M. Sintering Atmosphere Effects on Tensile Properties of Heavy Alloys. *Met. Mater. Trans. A* **1988**, *19*, 2467–2476. [[CrossRef](#)]

77. German, R.M.; Bose, A.; Mani, S.S. Sintering Time and Atmosphere Influences on the Microstructure and Mechanical Properties of Tungsten Heavy Alloys. *Metall. Mater. Trans. A* **1992**, *23*, 211–219. [[CrossRef](#)]
78. Rabin, B.H.; German, R.M. Microstructure Effects on Tensile Properties of Tungsten-Nickel-Iron Composites. *Met. Mater. Trans. A* **1988**, *19*, 1523–1532. [[CrossRef](#)]
79. Srikanth, V.; Upadhyaya, G.S. Effect of Tungsten Particle Size on Sintered Properties of Heavy Alloys. *Powder Technol.* **1984**, *39*, 61–67. [[CrossRef](#)]
80. Kennedy, E.W. *Microstructure, Fracture Characteristics, and Tensile Properties of Two Tungsten Heavy Alloys*; ARL-MR-269; Army Research Lab.: Aberdeen, MD, USA, 1995.
81. Fan, J.; Gong, X.; Qi, M.; Liu, T.; Li, S.; Tian, J. Dynamic behaviour and adiabatic shear bands in fine-grained W-Ni-Fe alloy under high strain rate compression. *Rare Met. Mater. Eng.* **2009**, *38*, 2069–2074. [[CrossRef](#)]
82. Zou, H.; Wang, Y.; Li, S. Effect of composition on microstructure and dynamic mechanical properties of W-Ni-Cu alloys. *Appl. Mech. Mater.* **2014**, *517*, 121–124. [[CrossRef](#)]
83. Ramakrishnan, K.N.; Upadhyaya, G.S. Effect of composition and sintering on the densification and microstructure of tungsten heavy alloys containing copper and nickel. *J. Mater. Sci. Lett.* **1990**, *9*, 456–459. [[CrossRef](#)]
84. Çalişkan, N.K.; Pehlivanoglu, M.K.; Bor, A.Ş. Effect of composition on the sintering behaviour and microstructure of W (90 wt.%)–Ni–Cu alloys. *Proc. Euro Powder Metall. Congr. Exhib. Eur. PM* **2007**, *2*, 405–410.
85. Johnson, J.L.; Upadhyaya, A.; German, R.M. Microstructural effects on distortion and solid-liquid segregation during liquid phase sintering under microgravity conditions. *Metall. Mater. Trans. B Process Metall. Mater. Process. Sci.* **1998**, *29*, 857–866. [[CrossRef](#)]
86. Liu, J.; German, R.M. Densification and shape distortion in liquid-phase sintering. *Metall. Mater. Trans. A* **1999**, *30*, 3211–3217. [[CrossRef](#)]
87. Lay, S.; Eustathopoulos, N.; Albert, C.H. Segregation of Fe during the sintering of doped W–Cu Alloys. *Scr. Mater.* **2003**, *49*, 237–242. [[CrossRef](#)]
88. Guillen, S.C. *The Journal of the Institute of Metals*; The Institute of Metals: London, UK, 1938; pp. 234–239.
89. Shen, J.; Campbell, L.; Suri, P.; German, R.M. Quantitative microstructure analysis of tungsten heavy alloys (W–Ni–Cu) during initial stage liquid phase sintering. *Int. J. Refract. Met. Hard Mater.* **2005**, *23*, 99–108. [[CrossRef](#)]
90. Das, J.; Kiran, U.R.; Chakraborty, A.; Prasad, N.E. Hardness and tensile properties of tungsten based heavy alloys prepared by liquid phase sintering technique. *Int. J. Refract. Met. Hard Mater.* **2009**, *27*, 577–583. [[CrossRef](#)]
91. Hong, M.; Noh, J.; Beak, W.H.; Kim, E.; Song, H.; Lee, S. A Study on the Improvement of the Sintered Density of W-Ni-Mn Heavy Alloy. *Met. Mater. Trans. A* **1997**, *28*, 835–839. [[CrossRef](#)]
92. Liu, H.; Cao, S.; Zhu, J.; Jinn, Y.; Chen, B. Densification, microstructure and mechanical properties of 90W–4Ni–6Mn heavy alloy. *Int. J. Refract. Met. Hard Mater.* **2013**, *37*, 121–126. [[CrossRef](#)]
93. Kim, D.K.; Lee, S.; Beak, W.H. Microstructural study of adiabatic shear bands formed by high-speed impact in a tungsten heavy alloy penetrator. *Mater. Sci. Eng. A.* **1998**, *249*, 197–205. [[CrossRef](#)]
94. Bose, A. Heavy Alloy Based on W-Ni-Mn. U.S. Patent US005603073A, 11 February 1997.
95. Belhadjhamida, A.; German, R.M. *High Performance Heavy Alloys by Alloying & Process Control*, AD A271129; US Army Research: Adelphi, MD, USA, 1993.
96. German, R.M. Lower sintering temperature tungsten alloys for space research. *Int. J. Refract. Met. Hard Mater.* **2015**, *53*, 74–79. [[CrossRef](#)]
97. Belhadjhamida, A.; German, R.M. *Effects of Atmosphere, Temperature, and Composition on the Densification and Properties of Tungsten-Nickel-Manganese*; Reannouncement with New Availability Information. No. AD-A-260373/6/XAB; Pennsylvania State Univ., Dept. of Engineering Science and Mechanics: University Park, PA, USA, 1992.
98. Zahraee, S.M.; Arabi, H.; Salehi, M.T.; Tamizifar, M. Effect of Mn/Ni ratio variation on microstructure of W-Ni-Mn alloy. *Powder Metall.* **2008**, *51*, 303–309. [[CrossRef](#)]
99. Pan, Y.; Xiang, D.; Wang, N.; Li, H.; Fan, Z. Mechanical milling-assisted spark plasma sintering of fine-grained W-Ni-Mn alloy. *Materials* **2018**, *11*, 1323. [[CrossRef](#)] [[PubMed](#)]
100. Pan, Y.; Ding, L.; Xiang, D. Microstructure evolution and mechanical properties of spark plasma sintered W–Ni–Mn alloy. *Trans. Nonferrous Met. Soc. China* **2017**, *27*, 1588–1593. [[CrossRef](#)]
101. Chen, B.; Cao, S.; Xu, H.; Jinn, Y.; Li, S.; Xiao, B. Effect of processing parameters on microstructure and mechanical properties of 90W–6Ni–4Mn heavy alloy. *Int. J. Refract. Met. Hard Mater.* **2015**, *48*, 293–300. [[CrossRef](#)]
102. Gao, Y.; Luo, B.H.; He, K.J.; Jing, H.B.; Bai, Z.H.; Chen, W.; Zhang, W.W. Mechanical properties and microstructure of WC-Fe-Ni-Co cemented carbides prepared by vacuum sintering. *Vacuum* **2017**, *143*, 271–282. [[CrossRef](#)]
103. Alvarado-Contreras, J.A.; Olevsky, E.A.; Maximenko, A.L.; German, R.M. Kinetics of shrinkage and shape evolution during liquid phase sintering of tungsten heavy alloy. *J. Mater. Sci.* **2013**, *49*, 1130–1137. [[CrossRef](#)]
104. Hu, K.; Li, X.; Qu, S.; Li, Y. Spark-Plasma Sintering of W-5.6Ni-1.4Fe Heavy Alloys: Densification and Grain Growth. *Metall. Mater. Trans. A Phys. Metall. Mater. Sci.* **2013**, *44*, 923–933. [[CrossRef](#)]
105. Zhou, C.; Yi, J.; Luo, S.; Peng, Y.; Li, L.; Chen, G. Effect of heating rate on the microwave sintered W–Ni–Fe heavy alloys. *J. Alloys Compd.* **2009**, *482*, L6–L8. [[CrossRef](#)]
106. Ramesh, K.T. On the localization of shearing deformations in tungsten heavy alloys. *Mech. Mater.* **1994**, *17*, 165–173. [[CrossRef](#)]

107. Kolsky, H. An investigation of the mechanical properties of materials at very high rates of loading. *Proc. Phys. Soc. Sect. B* **1949**, *62*, 676–700. [[CrossRef](#)]
108. Liu, J.; Upadhyaya, A.; German, R.M. Application of percolation theory in predicting shape distortion during liquid-phase sintering. *Metall. Mater. Trans. A Phys. Metall. Mater. Sci.* **1999**, *30*, 2209–2220. [[CrossRef](#)]
109. Wu, Y.; German, R.M.; Marx, B.; Suri, P.; Bollina, R. Comparison of densification and distortion behaviours of W-Ni-Cu and W-Ni-Fe heavy alloys in liquid-phase sintering. *J. Mater. Sci.* **2003**, *38*, 2271–2281. [[CrossRef](#)]
110. Mondal, A.; Upadhyaya, A.; Agrawal, D. Effect of heating mode and sintering temperature on consolidation. *J. Alloys Compd.* **2011**, *509*, 301–310. [[CrossRef](#)]
111. Humail, I.S.; Akhtar, F.; Askari, S.J.; Tufail, M.; Qu, X. Tensile behaviour change depending on the varying tungsten content of W-Ni-Fe alloys. *Int. J. Refract. Met. Hard Mater.* **2007**, *25*, 380–385. [[CrossRef](#)]
112. Hamid, Z.A.; Moustafa, S.F.; Daoush, W.M.; Mouez, F.A.; Hassan, M. Fabrication and Characterization of Tungsten Heavy Alloys Using Chemical Reduction and Mechanical Alloying Methods. *Open J. Appl. Sci.* **2013**, *3*, 15–27. [[CrossRef](#)]
113. Hwang, N.M.; Park, Y.J.; Kim, D.Y.; Yoon, D.Y. Activated sintering of nickel-doped tungsten: Approach by grain boundary structural transition. *Scr. Mater.* **2000**, *42*, 421–425. [[CrossRef](#)]
114. Prabhu, G.; Kumar, N.A.; Sankaranarayana, M.; Nandy, T.K. Tensile and impact properties of microwave sintered tungsten heavy alloys. *Mater. Sci. Eng. A* **2014**, *607*, 63–70. [[CrossRef](#)]
115. Li, Y.; Hu, K.; Li, X.; Ai, X.; Qu, S. Fine-grained 93W-5.6Ni-1.4Fe heavy alloys with enhanced performance prepared by spark plasma sintering. *Mater. Sci. Eng. A* **2013**, *573*, 245–252. [[CrossRef](#)]
116. Ayodele, O.O.; Shongwe, M.B.; Olubambi, P.A.; Obadele, B.A.; Langa, T. Hybrid Spark Plasma Sintering of Materials: A Review. *Int. J. Mater. Mech. Manuf.* **2018**, *6*, 360–364. [[CrossRef](#)]